AN ABSTRACT OF THE THESIS OF

Kenneth James Faase for the degree of Doctor of Philosophy in Mechanical Engineering presented on September 19, 1996. Title: Microstructures and Properties of Nb/Ti Multilayered Thin Films.

Abstract approved: Redacted for Privacy

William H. Warnes

The microstructures and properties of pure Nb, pure Ti and Nb/Ti multilayered thin films were studied. The films were deposited by DC magnetron sputtering and microstructurally characterized by Transmission Electron Microscopy (TEM), X-ray Diffraction (XRD) and Electron Microprobe Analysis. The critical superconducting properties, T_c, H_{c2}, and J_c, as well as the resistivity of the films were measured. A measured T_c of 9.0 K, a room temperature resistivity of 14 μΩ-cm and the expected BCC crystal structure in pure Nb films deposited at 200 °C indicate that the deposition process introduced a negligible amount of contamination and/or crystal disorder relative to bulk Nb. TEM images as well as XRD profiles showed all the Nb/Ti films had lattice parameters within 2% of expected BCC-Nb and HCP-Ti crystal structures. The resistivity of the films (10-50 μΩ-cm at room temperature) increased with an increasing density of Nb/Ti interfaces, yet all resistivities were below bulk alloy values. Unfortunately, the critical superconducting properties of all the Nb/Ti multilayered thin films were suppressed, with all J_c values at least a factor of two less than corresponding bulk alloys. Examination of the films over a range of bilayer periods (1.7 nm to 15,000 nm) showed the suppressed T_c and H_{c2} behavior to be in good qualitative and quantitative agreement with proximity effect models. The proximity effect models show that the depressed

superconducting properties of the films were a result of the film geometries (layer spacings and compositions).

MICROSTRUCTURES AND PROPERTIES OF Nb/Ti MULTILAYERED THIN FILMS

by

KENNETH JAMES FAASE

A THESIS

submitted to

Oregon State University

in partial fulfillment of
the requirements for the
degree of

Doctor of Philosophy

Completed September 19, 1996
Commencement June 1997

Doctor of Philosophy thesis of Kenneth James Faase presented on September 19, 1996

APPROVED:

Redacted for Privacy

Major Professor, representing Mechanical Engineering

Redacted for Privacy

Head of Department of Mechanical Engineering

Redacted for Privacy

Dean of Graduate School

I understand that my thesis will become part of the permanent collection of Oregon State University libraries. My signature below authorizes release of my thesis to any reader upon request.

Redacted for Privacy

Kenneth James Faase, Author

ACKNOWLEDGMENTS

"Congratulations!
Today is your day.
You're off to Great Places!
You're off and away!"

As I finish my graduate school experience, I find that I have lived and relived the words of Dr. Seuss's Oh! The Places You'll Go! many times. I have flown with the high fliers and watched the Boom Bands playing. I have played games I could not win and found myself alone in a Slump. Sometimes I relive the story over the course of a year, sometimes in the cycle of the moon, sometimes in the blink of an eye. Through the tellings and re-tellings of the story, Dr. William H. Warnes has been my Dr. Seuss. The creativity and color splash out at you on the first page of his books. As you continue to read from Bill's stories, you discover a magical combination of timeless wisdom and youthful playfulness. When you finish the story, you are left sense of warmth and kindness and an urge to read the book all over again. Thank you Bill.

"Simple it's not, I'm afraid you will find,
For a mind-maker-upper to make up his mind."

And in the places I go, I know I can always seek advice from Deana and my parents and family and friends who have helped me so many times before. Thank you.

"You'll get mixed up with many strange birds as you go."

Thanks to Kevin and Jeff for the life and times in the lab. Roberta Bigelow and Tracy (Her Queen Majesty of Nibbles) for the x-ray work. Jun Koike and Al Soeldner assisted with TEM work. Roger Nielsen performed the EMPA. Ralph Pombo and Joe Glaser made the films at Lawrence Livermore National Labs and the work was funded by Department of Energy, High Energy Physics Grant #DE-FG06-93ER40804.

TABLE OF CONTENTS

LIST OF FIGURES

LIST OF FIGURES (Continued)

LIST OF TABLES

LIST OF APPENDIX FIGURES

LIST OF APPENDIX TABLES

LIST OF ABBREVIATIONS AND SYMBOLS

a	Hexagonal crystal lattice parameter
a_o	Cubic crystal lattice parameter
APC	Artificial Pinning Center
at%	Atomic percent
BCC	Body Centered Cubic (crystal lattice)
BCS	Bardeen, Cooper and Schrieffer
BF	Bright Field
c	Hexagonal crystal lattice parameter
d_{FLL}	Spacing between fluxons in the flux line lattice
d_n	Normal layer thickness
d_s	Superconducting layer thickness
EMPA	Electron Microprobe Analysis
F_L	Lorentz force
FLL	Flux Line Lattice
F_p	Pinning force
GLAG	Ginzburg, Landau, Abrikosov and Gor'kov
H	Magnetic field
$H_{applied}$	Applied magnetic field
h_{c2}	Reduced upper critical field = $H_{c2\text{-film}}/H_{c2\text{-bulk material}}$
H_{c2}	Upper critical field
H_c	Thermodynamic critical field
HCP	Hexagonal Close Packed (crystal lattice)
H_o	Upper critical field at absolute zero
i	Subscript for the interface layer
J	Current density

LIST OF ABBREVIATIONS AND SYMBOLS (Continued)

J_c	Critical current density
k_B	Boltzmann constant
LHS	Left Hand Side
n	Subscript for the normal layers
Nb-Ti	An alloy of Nb and Ti
Nb/Ti	A multilayered thin film of pure Nb and pure Ti layers
NHT	No Heat Treatment
n_s	Density of superconducting electrons
RHS	Right Hand Side
s	Subscript for the superconducting layer
SAD	Selected Area Diffraction
t	Reduced temperature = $T/T_{c\text{-bulk material}}$
t_c	Reduced critical temperature = $T_{c\text{-film}}/T_{c\text{-bulk material}}$
T	Temperature
T_c	Critical temperature
TEM	Transmission Electron Microscope (microscopy)
wt%	Weight percent
XRD	X-ray diffraction
Δ	Superconducting energy gap
ξ_s	Superconducting coherence length
η	Electronic scattering parameter
κ	Ginzburg-Landau parameter
λ	Magnetic penetration depth
ϕ_o	Fluxon or 2.067×10^{-15} Tm^2
Ψ	Order parameter

DEDICATION

Dedicated to Mom and Dad.

MICROSTRUCTURES AND PROPERTIES OF Nb/Ti MULTILAYERED THIN FILMS

INTRODUCTION

Goal and Motivation

The goal of this thesis is to quantify and understand the property-microstructural relationships of various pure Nb and pure Ti multilayered thin films, which were designed to model conventional Nb47wt%Ti superconducting wire filaments. Previous microstructural-property studies of Nb-Ti have been extremely successful and consequently, Nb-Ti enjoys the role of being the most commonly used material in superconducting applications. Furthermore, increased performance will lead to substantial cost savings in the fabrication of future Nb-Ti superconducting devices. Thus this study is motivated by the potential for improved performance and/or cost savings in the Nb-Ti system through a better understanding of the property-microstructural relationships. Finally, further knowledge obtained in the Nb-Ti system could be used to enhance the performance of other superconducting material systems.

Basic Superconductivity

Superconductivity is a remarkable phenomenon which occurs in materials at extremely low temperatures (<20 K for most metals and metal alloys). When a superconducting material is cooled below its critical temperature, T_c, it undergoes a thermodynamic phase transition from a normal electrical conducting state to a state of zero electrical resistance, or a superconducting state. Two other critical criteria, the

critical magnetic field, H_c, and the critical current density, J_c, also determine the state of a superconducting material. On a three-axis plot, T_c, H_c, and J_c provide the limits of superconductivity along the temperature, magnetic field and current density axes, respectively. The three-way T, H, and J plot (Figure 1) describes a critical surface which separates the normal (above the critical surface) and superconducting (below the critical surface) states. The three parameters are interdependent so a superconductor may carry large amounts of current at a low temperature and/or magnetic field, but will be restricted to orders of magnitude less superconducting current near T_c and/or H_c.

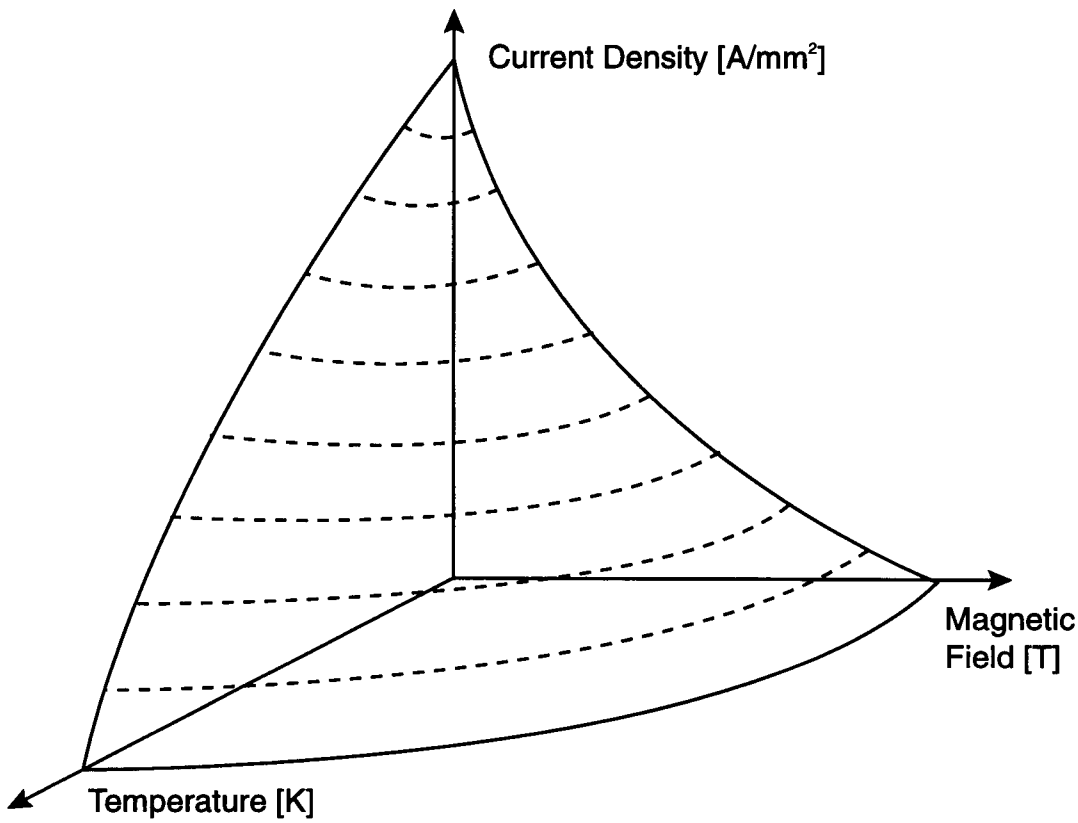

Figure 1. A schematic of a critical surface separating the superconducting phase (below the surface) and the normal phase (above the surface) as a function of temperature, magnetic field and current density.

The cornerstone theories of superconductivity are the Bardeen, Cooper and Schrieffer (BCS) theory [1] and the Ginzburg, Landau, Abrikosov and Gor'kov (GLAG) theories [2-4]. The BCS theory describes the fundamental behavior of superconductivity. According to the BCS theory, electrons of equal and opposite momentum at the Fermi level in a superconductor condense into electron-electron pairs, called Cooper pairs, when the superconductor is cooled below its critical temperature. The Cooper pairs form an attractive interaction through the exchange of a 'virtual phonon' (see Figure 2). Although the formation of the Cooper pair increases the kinetic energy of the system, this increase is outweighed by the decrease in the potential energy in the system due to the attractive binding, resulting in a decrease in the total energy of the system. This reduction in the total thermodynamic energy of the system, which corresponds to the energy needed to break a Cooper pair, forms an energy gap, Δ, in the band structure of the superconductor at the fermi level. The critical temperature of a superconductor has been directly related to this energy gap (measured independently of T_c with calorimetric and electromagnetic absorption experiments) as

$$T_c = 2\Delta / (3.52\, k_B) \qquad \text{Equation 1}$$

where k_B is the Boltzmann constant. Similar to the effects of temperature, increasing the magnetic field of a superconductor increases the kinetic energy of the Cooper pairs. As the field increases to a value of H_c, the increase in kinetic energy approaches the decrease in potential energy of the Cooper pair; upon reaching H_c where the additional kinetic energy breaks the Cooper pair and destroys superconductivity. Thus, the critical temperature and critical field, which are related to the band structure, are a function of the bulk composition of the superconducting material according to BCS theory. H_c and T_c are related to one another through the expression

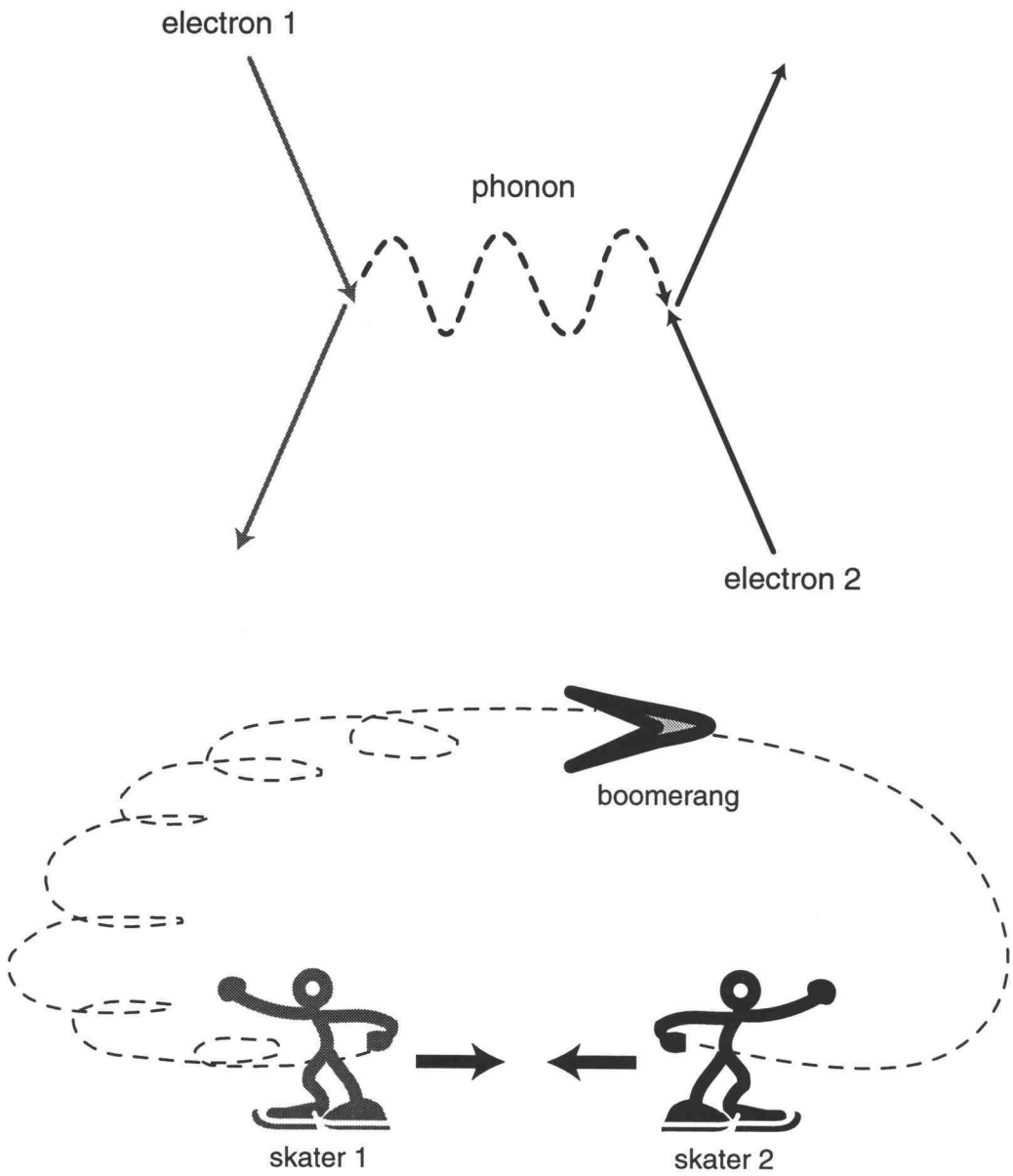

Figure 2. A Feynman diagram of the exchange of a "virtual phonon" between electrons in a Cooper pair. Before the exchange, electrons 1 and 2 have an equal and opposite momentum. The exchange of the phonon symmetrically scatters the electrons, so that after the exchange the electrons again have an equal and opposite momentum. The attractive nature of this exchange is analogous to two ice-skaters throwing a boomerang to one another. As skater 1 throws the boomerang in a direction opposite to skater 2, the force of the throw accelerates skater 1 towards skater 2. Also, as the boomerang is caught by skater 2, the momentum of the boomerang pushes skater 2 towards skater 1, thus producing an attractive interaction between the two skaters [5].

$$H_c(T) = H_o\left[1-\left(\frac{T}{T_c}\right)^2\right]$$ Equation 2

where H_0 is the critical field at absolute zero. An exception to this rule occurs when the size scale of the superconducting system is extremely small and is subject to the proximity effect (see below).

In the GLAG theories, Ginzburg and Landau used a quantum mechanical wave function called the order parameter, Ψ, to describe the spatial variation of superconductivity such that $|\Psi(x)|^2 = n_s$, where x is a position in the superconductor and n_s is the density of superconducting electrons at that point. The theories also describe the coherence length, ξ_s, of a superconductor which is defined as the length scale over which Ψ can change (i.e. the thickness of the interface between the normal and superconducting phases). Abrikosov [3] extended the Ginzburg Landau theory by predicting the existence of two types of superconductors and the Flux Line Lattice (FLL). Type I and Type II superconductors are defined through the Ginzburg Landau parameter, κ, where

$\kappa = (\lambda/\xi_s) < 1/\sqrt{2}$ Type I Equation 3

$\kappa = (\lambda/\xi_s) > 1/\sqrt{2}$ Type II Equation 4

λ is the penetration depth of magnetic flux into the bulk of the superconductor and ξ_s is the coherence length. Usually alloy materials, Type II superconductors have a negative surface energy between the superconducting and normal states at high magnetic fields, as opposed to Type I superconductors which are usually pure metals and have a positive surface energy.

As the applied magnetic field of a Type II superconductor increases, magnetic flux enters the bulk of the material in an array of normal state, quantum flux particles, or

fluxons, called the Flux Line Lattice (FLL) (see Figure 3). The cylindrical fluxons, with a diameter of $2\xi_s$, arrange themselves in a hexagonal lattice with a spacing of

$$d_{FLL} = \sqrt{\frac{2\phi_o}{\sqrt{3}H_{applied}}} \qquad \text{Equation 5}$$

where ϕ_0 is the magnetic flux associated with a single fluxon (2.067×10^{-15} Tm^2) and the field is given in units of Tesla. The presence of the FLL and the accompanying negative surface energy increase the critical magnetic field of a superconductor from H_c to H_{c2} through the relationship

$$H_{c2} = \sqrt{2}\kappa H_c. \qquad \text{Equation 6}$$

The coherence length, ξ_s and H_{c2} are related by the expression

$$H_{c2} = \frac{\phi_o}{2\pi\xi_s^{\,2}}. \qquad \text{Equation 7}$$

The FLL is a key aspect of flux pinning theories which describe the physical foundations of the critical current density in a superconductor. According to basic flux pinning theories, the J_c of a superconductor is controlled by the interaction between the transport current, the FLL and the local microstructure in a superconductor [6]. When a transport current is applied to a Type II superconductor in high magnetic field, a Lorentz force (per volume), F_L, is produced on the FLL such that

$$\vec{F}_L = \vec{J} \times \vec{H}_{applied} \qquad \text{Equation 8}$$

where J is the current density and $H_{applied}$ is the applied magnetic field as shown in Figure 3. At current densities below J_c, a pinning force, F_p, acts on the FLL equally and opposite to the Lorentz force, thus preventing flux motion. The pinning force is due to local variations in the microstructure of the superconductor (precipitates, compositional

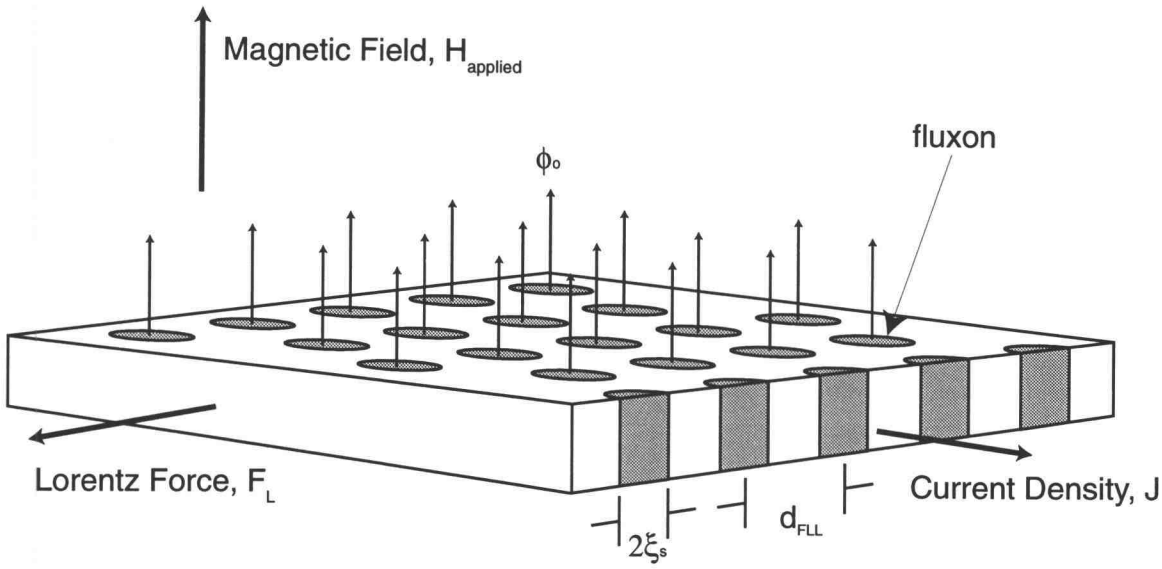

Figure 3. A diagram of the hexagonally spaced flux line lattice in the bulk of a Type II superconductor. The diagram also shows the direction of the Lorentz force for the case of current density perpendicular to magnetic field.

gradients, grain boundaries and atomic defects) which are energetically favorable sites for the individual fluxons in the FLL. The term "flux pinning" refers to the fluxons sitting on these energetically favorable sites. As the critical current reaches J_c, the Lorentz force exceeds the pinning force in the superconductor resulting in flux motion which induces a voltage in the superconductor, thus destroying the zero resistance state.

Presently two primary flux pinning theories exist, the core-pinning theory and surface pinning theory [7]. The core pinning theory is based on the fact that there is a reduction in the free energy of the FLL/superconducting system when an individual fluxon moves from a superconducting region to a normal region (e.g. non-superconducting precipitate, grain boundary). Core-pinning theory predicts the optimal geometry for maximum flux pinning would be a matrix of cylindrical normal state regions aligned parallel to the magnetic field which match both the fluxon diameter and

spacing. Surface pinning theory suggests that fluxons are pinned by normal surface-area regions which act as barriers that prohibit the transmission of superconducting electrons. Thus according to surface pinning-theory, the ideal geometry for maximum flux pinning would be atomic monolayers of pinning planes aligned parallel to the FLL, which match the spacing of the fluxons in the FLL.

The Nb-Ti System

Nb-Ti superconductors are the most widely used in superconducting applications. The driving force behind the development of Nb-Ti superconductors and one of the principal applications of the alloy has been magnet wire for large-scale nuclear particle accelerators. Other spin-off, but nevertheless important applications include, magnetic energy storage, magnetic resonance imaging, magnetic separation and research magnets. Nb-Ti is common to all of these applications principally due to its high critical current density and ease of fabrication. Wires with high critical current densities provide higher, more uniform magnetic fields in solenoids at a lower cost than wires with low critical current densities.

The push for higher critical current densities has been the principal focus of research in Nb-Ti superconductors for over twenty years [8-14]. Despite the tremendous efforts and successes of this research, large discrepancies still exist between the theoretical limits and experimentally achieved values of J_c in the Nb-Ti system due in part to an incomplete understanding of the basic pinning mechanism.

To understand the source of these discrepancies, one needs only to look at the processing steps and final microstructure of the Nb-Ti wire composites. Nb-Ti wire composites are fabricated with an extremely intensive thermo-mechanical processing schedule where the wire will see total area reductions on the order of 10^6:1 and 4-6 heat

treatments [14]. The heat treatments produce a two-phase microstructure, Figure 4, while the cold work provides nucleation sites and microstructural refinement. The final microstructure, Figure 5, consists of thin (2-4 nm) ribbons of α-Ti randomly woven in a highly strained β-Nb-Ti matrix structure [12]. These ribbons are directly responsible for flux pinning and the high current densities in the Nb-Ti wires.

Due to the size scale of the α-Ti pinning structure, the microstructure can only be imaged by TEM. Although TEM imaging of the microstructure has been quite successful in uncovering many of the present microstructural-property relationships in Nb-Ti, this work is extremely difficult in terms of both sample preparation and sample imaging and has been successful in only a few labs throughout the world. Finally, there is little control of the final microstructure and its random nature does not lend itself to the modeling of the complex interactions between the microstructure and the FLL. Thus, the question of which flux-pinning mechanism and therefore which pinning geometry is optimal in Nb-Ti superconductors still remains unanswered.

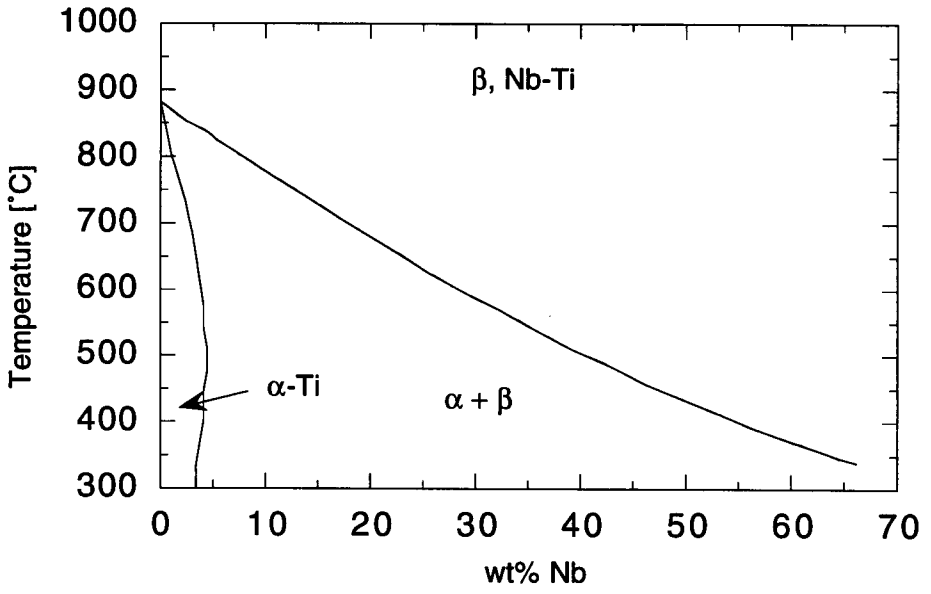

Figure 4. The Nb-Ti phase diagram [24].

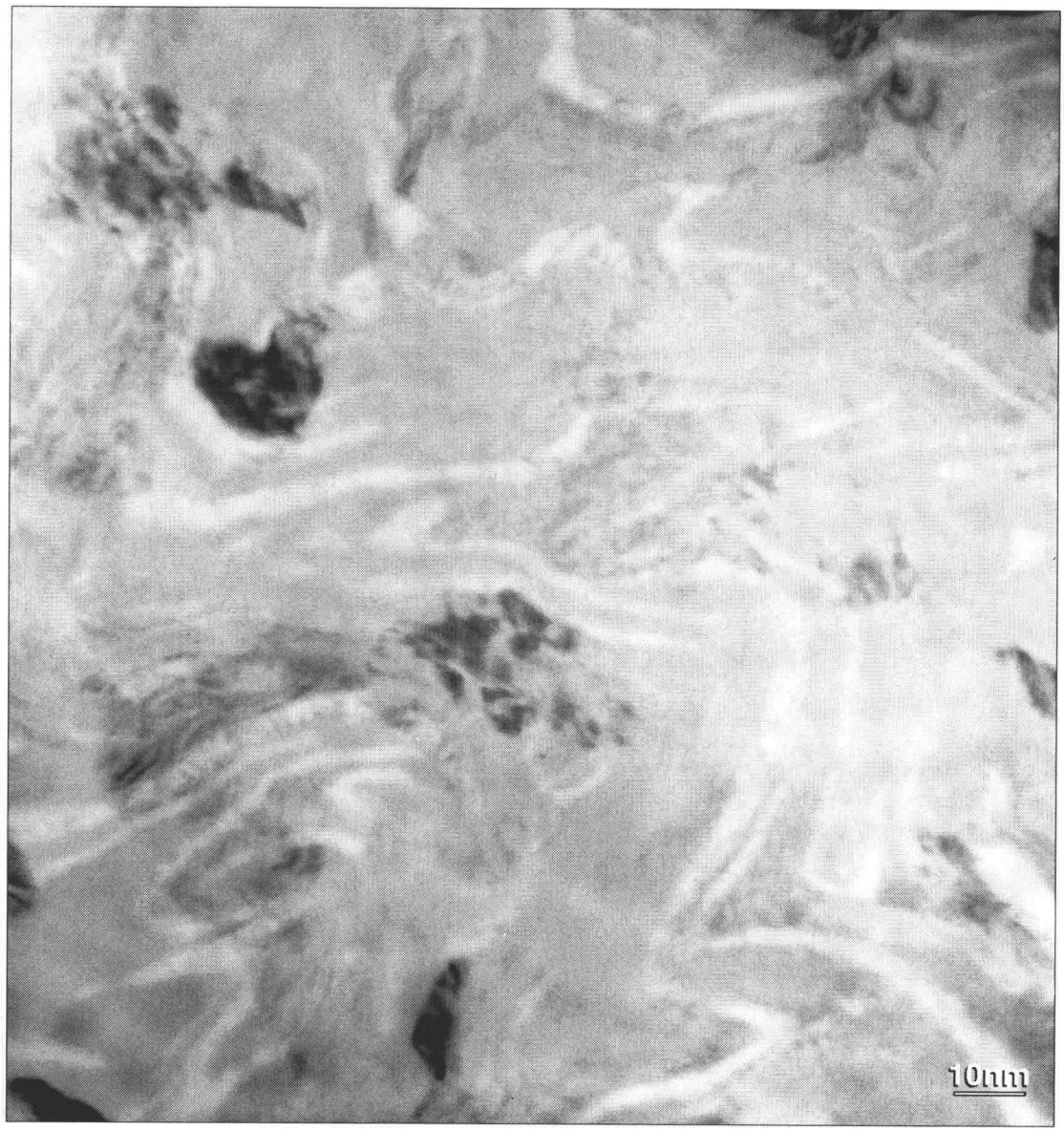

Figure 5. A bright field TEM micrograph of a conventionally processed Nb47wt%Ti wire composite in transverse cross section. The white ribbons in the micrograph are α-Ti precipitates. The precipitates are the flux-pinning centers which produce the high critical current densities in the wires.

Limitations in the control over the final microstructure of conventionally processed Nb-Ti wire composites led to the development of Artificial Pinning Center (APC) Nb-Ti composites [15-23]. The APC approach is to assemble mechanically the desired pinning geometry at a large size and then to reduce the dimensions of the composite to the desired pinning dimensions by wire drawing and extrusions. The principal advantage of the APC approach is the potential for control over the percent of pinning material in the cross section. Conventional wire composite studies show a direct relationship between the volume fraction of α-Ti and J_c, up to their thermodynamic limit of ~25 volume fraction α–Ti [14]. APC wire composites, which are not limited to a maximum volume fraction of pinning material, hold the highest critical current densities (3780 A/mm^2 at 4.2 K, 5 T) of any round wire composite to date [16]. Unfortunately, the final microstructure of the APC composites lose all of their original pinning geometry, resulting in randomly oriented microstructures which are very similar in pin geometry to the conventionally processed wire composites [15]. An alternative approach to studying FLL/pinning would be to fabricate uniform microstructures using thin film deposition techniques.

Nb/Ti Multilayered Thin Films

The Nb-Ti system is a good candidate for multilayered thin film deposition. At deposition temperatures (<200 °C), the Nb-Ti phase diagram, Figure 4, shows near complete insolubility of Nb in Ti, thus preventing the formation of possibly undesirable intermetallic compounds. Nb and Ti have similar lattice parameters which reduces lattice mismatch strains during film deposition. Furthermore, interdiffusion rates between Nb and Ti are extremely low which suggests that the superlattice structure of the multilayered films should be thermally stable with sharp atomic interfaces. The field of

multilayer film fabrication has matured to the point that it is possible to produce highly crystalline, uniform, parallel layers of thicknesses on the order of nanometers or less. This makes Nb/Ti multilayer film fabrication an ideal candidate for the design of model microstructures for superconducting flux pinning studies. These size scales are also important to the proximity effect of superconductivity, which determines the T_c and H_{c2} of the superconductor and therefore influences the J_c of the film.

Proximity effect theory describes the behavior of superconducting/normal thin film systems as the dimensions of the superconducting and normal layers approach the coherence length, ξ_s [25-28]. Macroscopically, proximity effect behavior is associated with a reduction in T_c (and/or H_{c2} and J_c) as the bilayer period, Λ, approaches ξ_s. The physical foundations of this behavior can be seen microscopically by looking at the profile of the density of superconducting electrons, n_s, in superconducting/normal multilayers. These macroscopic and microscopic proximity effect behaviors are shown in Figures 6 and 7 respectively for the Nb/Ti multilayer system, where ξ_s of Nb is ~100-180 nm. At Point A of Figure 6, the bilayer period is greater than ξ_s and the T_c of the Nb/Ti system approaches the T_c of pure, bulk Nb. Microscopically, this behavior is identical to bulk behavior as n_s increases from 0 to 1 over the length ξ_s as seen in Figure 7a. When $\Lambda \leq \xi_s$ in the Nb/Ti bilayer, the density of superconducting electrons is unable to reach bulk values, as seen in Figure 7b. Although superconductivity still exists in the system, the kinetic (thermal) energy needed to break the Cooper pairs is decreased by the decrease in n_s, which is associated with a lower T_c as seen at Point B in Figure 6.

In the Nb-Ti system [29-35], as well as the Nb-Zr [36-42], Nb-Ta [43-44] and other systems, the alloy is a stronger superconductor than the two pure constituents. This creates a special case where a trilayer model is needed to properly describe the proximity effect in the limit of small Λ. Macroscopically, as Λ approaches zero, the properties of the film approach the properties of the Nb-Ti alloy, as seen at Point C in Figure 6.

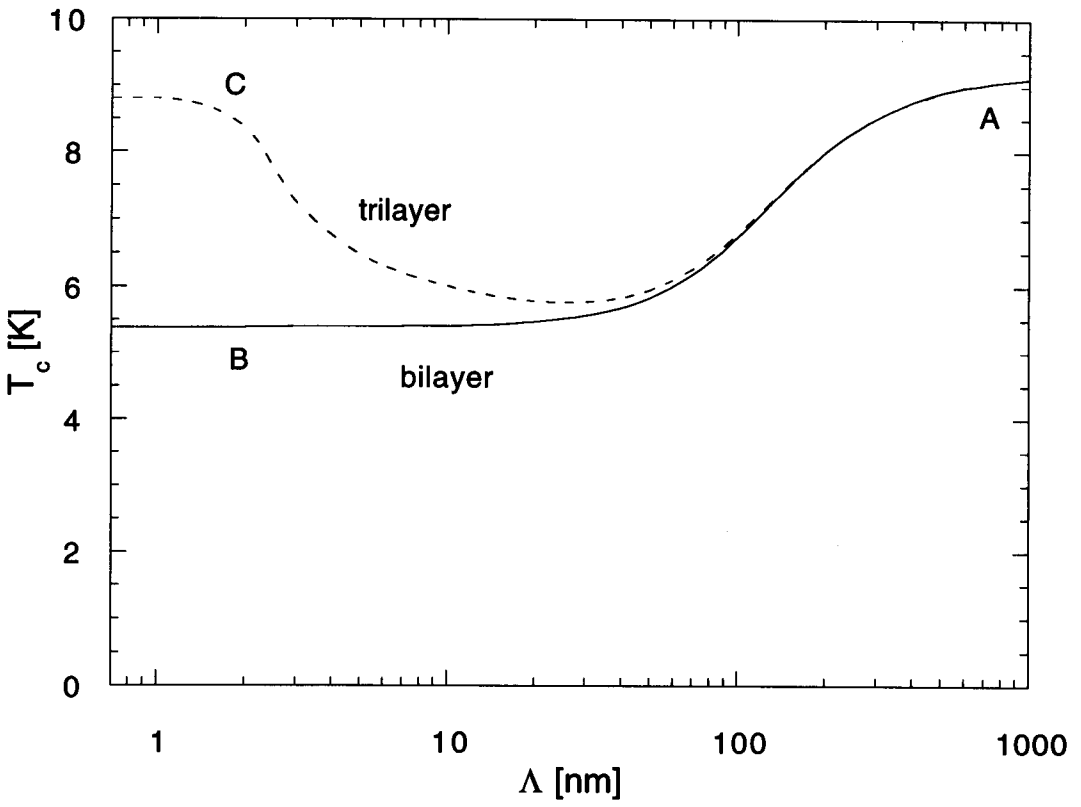

Figure 6. Proximity effect calculations of T_c versus Λ in the Nb-Ti system based on the proximity effect model of Ledvij et al. [28]. The bilayer curve was calculated by setting the interface layer to zero thickness. The points A-C correspond to Figures 7a-c, respectively.

Microscopically, as the period of the Nb/Ti multilayer approaches sub-nanometer size scales, any interfacial mixing of the Nb and Ti layers due to interdiffusion, interface roughness and/or non-ideal film deposition results in an alloy layer of Nb-Ti such that the bilayer period may be defined as

$$\Lambda = d_s + d_n + 2d_i \qquad \text{Equation 9}$$

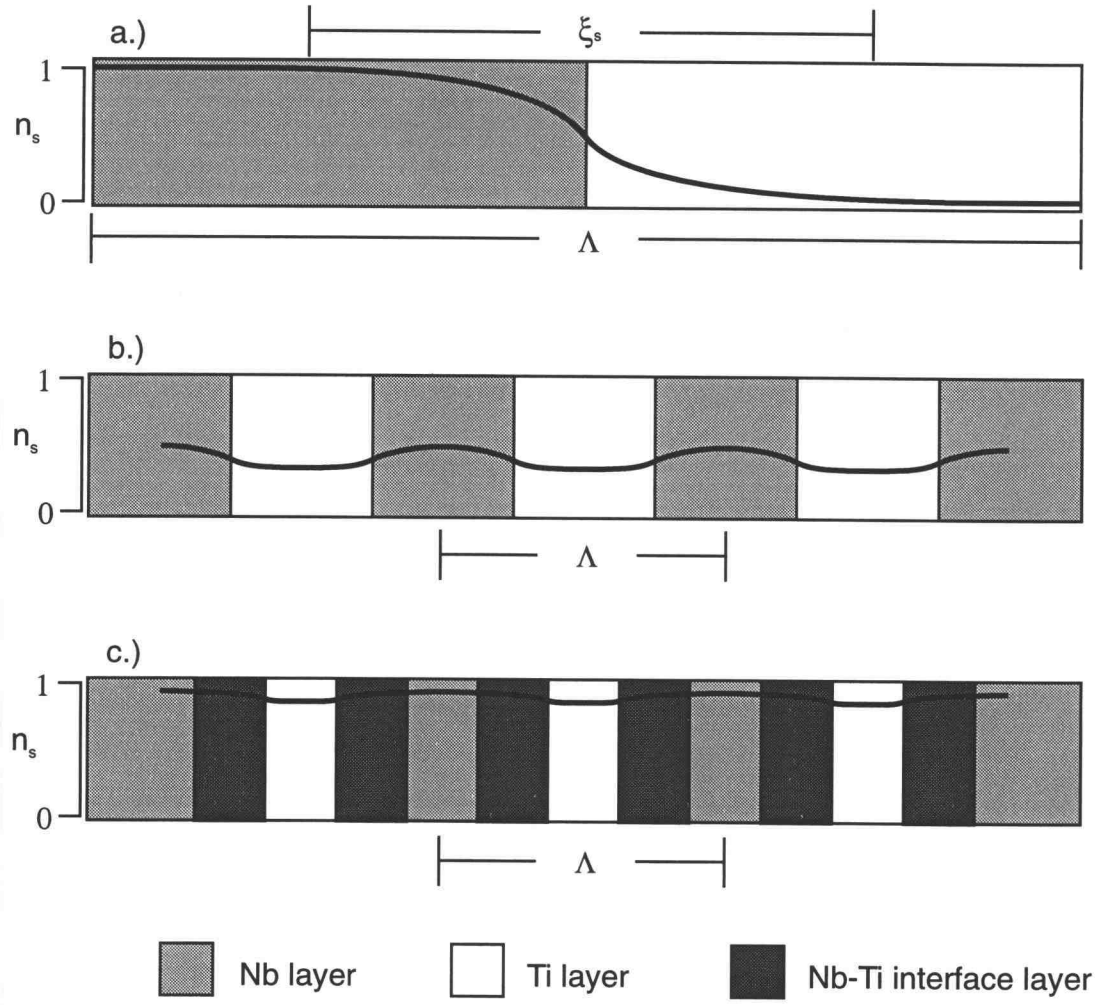

Figure 7. Profiles of the density of superconducting electrons in various multilayer configurations; a.) $\Lambda >> \xi_s >> d_{interface}$, b.) $\Lambda \leq \xi_s$ in a bilayer, c.) $\Lambda \leq \xi_s$ in a trilayer. Figures 7a-c correspond to the points A-C in Figure 6, respectively.

where d_i is the thickness of a Nb-Ti interface layer that exists between the pure Nb, d_s, and pure Ti layers, d_n, as seen in Figure 7c. Not only does the Nb-Ti alloy account for a substantial fraction of Λ at these size scales, the presence of the alloy layer increases the superconducting/normal layer thickness ratio, thus creating more bulk-like superconductor geometries. Furthermore, the coherence length of a Nb-Ti alloy is less than pure Nb, so n_s and therefore T_c may increase to bulk values. These predictions are in

good agreement with the study of Meingast [13] in conventionally processed Nb-Ti wires. Meingast concluded that as the scale of the microstructural inhomogenities fell below the coherence length of the superconductor, the properties of the system would return to homogeneous bulk properties.

Two studies on Nb/Ti multilayered thin films have been published, Sato [29] and Qian [30]. Sato deposited several different series of Nb/Ti films with bilayer periods between 0.2-10 nm and d_s/d_n thickness ratios between 3 and 1/3. Qian et al. looked at a single series of Nb/Ti films with a larger bilayer period range, 0.6-625 nm. Neither study reported any J_c values, although both studies provided T_c versus Λ plots, (Figure 8). The T_c versus Λ plots did not agree with each other quantitatively, although each showed proximity effect depressions at bilayer periods around 10 nm. Both studies also showed an increase in T_c to that of bulk Nb-Ti as Λ approached zero. Sato developed a proximity effect model which properly accounts for the depression in T_c over the range of Λ in the study. Unfortunately, the model does not properly predict the return of T_c to that of bulk Nb as the trilayer period approaches infinity. Ledvij et al. [28] developed a trilayer proximity effect model that quantitatively fits the non-monotonic behavior of the Qian Nb/Ti T_c versus Λ data and shows the proper limiting behavior of T_c, ξ_s, and other parameters as a function of Λ.

Another study, by Obi et al. [31], examined the superconducting properties of NbTi/Ti and NbTi/Nb films using bilayer periods from 5-200 nm. As in the Nb/Ti films, proximity effect reduces the T_c of these films, although the T_c depression of the Nb-rich $(Nb_{65}Ti_{35})$/Nb films is smaller than the depression of the Ti-rich $(Nb_{28}Ti_{72})$/Nb films or the Nb/Ti films of Sato and Qian. The study also includes H_{c2} versus Λ data which fit the proximity effect model of Takahashi and Tachiki [45-46]. The Takahashi and Tachiki proximity effect model, which predicts the possibility of the H_{c2} in films being higher than the H_{c2} of either of the constituent layers, was also found to be in excellent agreement with H_{c2} data from NbTi/Nb thin films of Karkut et al. [34].

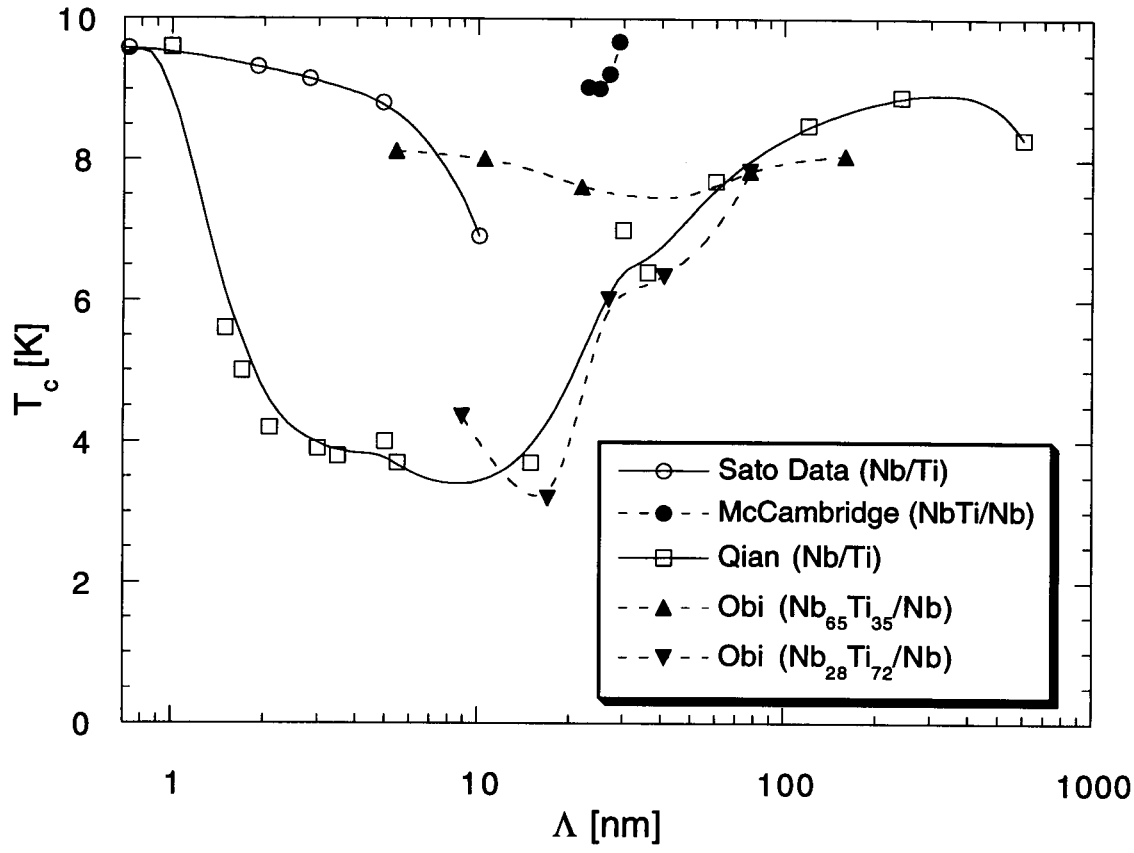

Figure 8. Experimental T_c versus Λ from the literature. The lines in the plot are included to visually connect individual data points.

Another study of NbTi/Nb films by McCambridge et al. [32] examines the effects of T_c, H_{c2} and J_c in a series of films with 20 nm Nb47wt%Ti layers coupled with Nb layers ranging from 3-17 nm. McCambridge et al. found no reductions in the T_c of the films, but did report substantial H_{c2} depressions at low temperatures which they concluded were consistent with proximity effect theory. The principal focus of the study was the critical current properties of the films. Record J_c's of 8,000 A/mm^2 (4.2 K, 5 T) were reported with high critical current densities which were directly attributed to the geometry of the multilayer structure.

In summary, there exists a wide range of superconducting properties in the Nb/Ti and NbTi/Nb thin films. Although most of variations in the properties can be explained by the proximity effect, the models as presented only agree qualitatively, with liberal use of "free" input parameters. Also common to these studies is incomplete or non-existent information on the microstructure of the films. This leads to the conclusion that the variations in the properties of these films may be due to variations in the microstructural quality of the films and not just the film geometries.

In an attempt to separate the effects of the geometry (proximity effect) and the microstructural quality (i.e. contamination levels, crystal order) on the superconducting properties of Nb/Ti multilayered thin films, this study emphasizes a complete characterization of *both* the microstructure and the properties of a series of pure Nb, pure Ti and Nb/Ti multilayered thin films. The pure metal films provide a direct assessment of the film quality, relative to bulk materials, by removing the possibility of degradation in the properties of the films due to the proximity effect. Characterization of the pure metal films also provides input values (resistivity, T_c and H_{c2}) that remove the need for "fitting parameters" in the proximity effect models. The use of complementary microstructural characterization techniques, Transmission Electron Microscopy (TEM), Electron Microprobe Analysis (EMPA) and X-Ray Diffraction (XRD), provides a complete picture of the structure, geometry and composition of the Nb/Ti films that cannot be obtained by a single technique, but is essential to properly quantifying the microstructure-property relationships of the films.

EXPERIMENTAL PROCEDURE

Sample Fabrication

The thin films were fabricated in the Vacuum Processing Labs at Lawrence Livermore National Lab. The films were deposited on 4" diameter Si <100> p-type substrates using a DC magnetron sputtering system. Two Torus 10 sputtering guns were used, one for the Ti layers and one for the Nb layers. The sputtering rates were 1.5 Å/s and 1.7 Å/s for the Nb and Ti layers, respectively. Before deposition, the deposition chamber was evacuated to 10^{-7} torr. Residual gas analysis performed during this initial evacuation showed negligible oxygen content. The samples were deposited in 3-5 millitorr with 99.995% pure Ar. Two different substrate deposition temperatures were used, an ambient (20 °C < T <115 °C) temperature and 200 °C. In each deposition run, up to nine samples were deposited simultaneously to provide sample redundancy.

Film Design

The films studied in this work can be logically divided into four sets. The film design and deposition parameters are listed in Table 1. The first set of films were pure Nb and pure Ti, single metal films. These films were used to assess the quality of the deposition process. Also, the superconducting properties of the single metal films were used as input parameters for the proximity effect models. The second set of films was a series of pure Nb/pure Ti multilayered thin films. The Nb/Ti multilayer films were designed to model conventional superconducting filaments by creating a two-phase microstructure with a bulk composition of Nb47wt%Ti. To test the effects of the

Table 1. Film design and deposition parameters.

Film Set	d_S [nm]	material	d_n [nm]	material	Bilayer period, Λ [nm]	Number of layers	Total film thickness [μm]	Deposition Temperature [°C]
pure Ti	0	x	10.7	Ti	10.7	300	3.21	115 °C
pure Nb	17.8	Nb	0	x	17.8	125	2.23	115 °C
pure Nb	17.1	Nb	0	x	17.1	280	4.80	200 °C
Λ=1.7 nm*	0.6	Nb	1.1	Ti	1.7	1200	2.00	200 °C
Λ=17 nm	6.1	Nb	10.7	Ti	16.8	120	2.02	115 °C
Λ=170 nm*	61	Nb	107	Ti	168	12	2.02	200 °C
Λ=15,000 nm	4,700	Nb	10,000	Ti	14,700	1	14.7	200 °C
(Nb/Ti)/Ti*	3.2/1.1	Nb/Ti ML	26.8	Ti	51.5	65	3.35	200 °C

* These films had a 10 nm Ti buffer and cap layer to reduce the lattice mismatch with the Si substrate and to prevent post-deposition contamination.

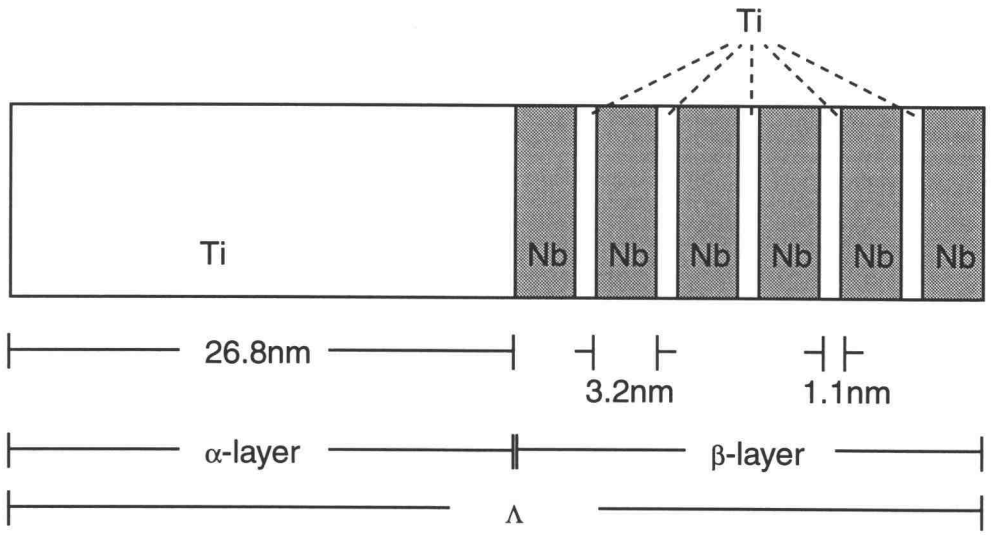

Figure 9. The design of the (Nb/Ti)/Ti "pseudo-alloy" multilayered thin film.

proximity effect, the bilayer period of the Nb/Ti multilayer films ranged from 1.7 nm to 15,000 nm. The Λ=17 nm film was designed to have layer thicknesses that would match the spacing of fluxons at a field of 5 T. The third set of films was designed to use the proximity effect to create a "pseudo-alloy" of Nb/Ti by depositing very thin ($d_{s,n} << \xi_s$) pure metal layers as a multilayered sublattice of Nb/Ti (β-layer) in a superlattice with relatively thick Ti layers (α-layer) as shown in Figure 9. The purpose of the pseudo-alloy (Nb/Ti)/Ti film set was to create alloy layers without using expensive alloy sputter targets. The fourth set of films was another attempt at creating alloy multilayers by interdiffusing the pure Nb/pure Ti layers of the second film set (Λ=17 nm) with a series of heat treatments of 1-10 hours between 300-600 °C [35]. The heat treated films also provided a check of the thermal stability of the films as well as the formation of a variable thickness Nb-Ti interface layers used in the Ledvij [28] proximity effect model.

Microstructural Characterization

The microstructures of the films were characterized with EMPA, XRD and TEM Bright Field (BF) and Selected Area Diffraction (SAD). TEM was performed on a Philips CM12 TEM/STEM with an optimal spatial resolution of 0.14 nm. The SAD images were all taken with a camera constant of 770 mm and indexed with the same procedure as described in Hirsch et al. [47]. Microprobe analysis was performed on a Cameca SX50 at an accelerating voltage of 20 kV, a beam current of 15 nA. All of the EMPA measurements were calibrated with pure Nb and pure Ti standards.

TEM samples were examined in both the plan view (a direction parallel to the normal of the film planes) and transverse view (a direction perpendicular to the normal of the film planes). Image analysis measurements of the individual layer thicknesses and the average grain sizes measurements were performed on the transverse and plan view

sections, respectively. The grain diameter measurements were the average of thirty or more grains in plan view, assuming circular grains. The reported layer thickness measurements were the average of ten measurements. To determine the composition of the film from TEM measurements, the thickness ratio d_s/d_n was taken as the atomic fraction Nb in the film. The atomic fractions were converted into weight fractions and compared to EMPA measurements of the composition.

Transverse view samples were prepared for TEM using a technique adapted from Wall [48]. The film/substrate was cleaved into rectangular strips ~3 mm X 30 mm and cleaned in an ultrasonic acetone bath. The film faces were epoxied together with aluminum foil in the film/epoxy/film interface. Aluminum strips were epoxied onto the outside silicon/film/epoxy composite. The aluminum was added for mechanical support during subsequent processing steps. The composite was then sectioned perpendicular to the plane of the films into ~300 μm thick slices with a low-speed diamond saw. Each side of the sample was then mechanically polished with diamond paper to a finish of 0.5 μm and a thickness of ~50-75 μm. Subsequent processing was similar to Wall [48] with mechanical dimpling of one side to a minimum sample thickness of 0-5 μm followed by low angle (7-11°) ion milling using a milling stage that preferentially mills in a direction perpendicular to the plane of the films [49].

The plan view TEM sample preparation started with 3 mm X 3 mm cleaved samples of film/substrate. The substrate side of the samples were mechanically polished parallel to the plane of the films to ~25-50 μm in thickness. Subsequent processing, dimpling and milling, was the same as the transverse samples (except for the use of direction milling).

XRD was performed on a Seimens Diffraktometer D5000 using a $Cu_{K\alpha 1}$ source. The XRD data was taken over a range of 1-140° 2θ, using 0.02° 2θ steps, and 1-20 second count times per step. The raw data was averaged over nine, 0.02° steps. The 2θ value used to calculate the lattice spacings was the maximum in the diffraction peak. The cubic

lattice parameters listed are the extrapolated value of $\sin^2\theta=1$ on a lattice parameter versus $\sin^2\theta$ plot [50]. In the case of the heat treated thin films where only two diffraction peaks were observed, the lattice parameter was taken as the average lattice parameter of the two peaks. An analytical technique [50] was used to calculate the lattice parameters of the HCP phases. The bilayer period, Λ, was calculated from the low angle superlattice peaks as $\Lambda = \lambda/\Delta\theta$, where λ is the wavelength of the x-ray source, and $\Delta\theta$ is the average angular difference between the low order peaks due to the superlattice.

Electromagnetic Characterization

The T_c of the films was measured by AC susceptometry. Two small coils were axially aligned above and below a rectangular piece of film ~10 mm X 30. The sample was oriented such that the normal to the film plane was parallel to the axes of the two coils. A lock-in amplifier produced an alternating current in one of the coils. Above the transition temperature of the sample, the field from the excitation coil produced a magnetic field large enough to be read by the pick-up coil. Below T_c, the magnetic shielding of the sample reduced the signal to the pick-up coil, thus producing a measurable critical temperature transition. The temperature control system was monitored by a Cernox sensor and maintained by a heater coil wrapped around the sample holder/coil assembly. The temperature was calibrated with two "witness point" coils. One witness point coil was wrapped around a piece of pure Nb (T_c = 9.2 K) and the other around a piece of pure Pb (T_c = 7.2 K). As the temperature decreased below the T_c of each witness point, the signal from that coil was removed due to the screening currents of the calibrated superconductor, producing a small drop in the overall signal to the pick-up coil. The two measured witness points and the measured boiling point of He (4.2 K) were plotted against their respective observed values to form a calibrated temperature curve for

each sample measured. The reported T_c of the sample was taken from the calibrated temperature curve at a point which corresponded to 50% of the sample's measured temperature transition.

The same rig contained a small four-point probe which was used to resistively measure the H_{c2} and I_c transitions, as well as measuring resistivities as a function of temperature of the samples. For the H_{c2} and I_c measurements, the applied field and current were perpendicular to each other and were parallel to the plane of films. In the H_{c2} measurement, a 25 mA constant current (~1-3 A/mm^2) was applied to the sample. The field was ramped up until a resistive transition was found and the reported H_{c2} was taken at 50% of the transition. The I_c measurement used a 5 $\mu V/cm$ criterion based on the voltage tap gauge length of 20 mm.

The resistivity of the films was calculated from resistance measurements at a given temperature (either 12 K or 300 K) with input currents ranging from $\pm$100 mA. Resistance measurements of a bare Si substrate as a function of temperature were made and converted to resistivity measurements based on the dimensions of the Si specimen. Using a model of parallel current sharing, the resistance of the Si was subtracted from the total resistance of the film/substrate to give the resistance of the film. The dimensions of the film were then used to convert the resistance of the film to resistivity.

RESULTS

Microstructural Characterization

Pure Metal Films

In all cases the TEM micrographs, SAD patterns and XRD profiles show the films to be highly textured, with columnar grains oriented in the same crystallographic direction. Evidence of the texturing can be seen in the TEM micrographs by comparing the plan view and transverse view of the pure Nb and pure Ti films in Figures 10-11. The transverse view micrographs of the Nb and Ti films (Figures 10a-d) show columnar grains about 10-60 nm in diameter growing perpendicular to the Si substrate. The SAD patterns in the transverse view (Figures 11a-d) show a single crystallographic set of planes, BCC{110} and HCP{0001}, for the pure Nb and pure Ti films, respectively. The plan view bright field images show an equiaxed grain structure with BCC and HCP ring patterns found in the SAD patterns for the pure Nb and pure Ti films, respectively.

Further evidence of texturing, found in all of the films, was the dominant XRD peaks around atomic plane spacings of 2.34 Å and 1.17 Å. These two atomic plane spacings represent the Nb-BCC{110}/Ti-HCP{0002} and Nb-BCC{220}/Ti-HCP{0004} atomic planes with bulk-value lattice spacings [50] of 2.338 Å / 2.342 Å and 1.169 Å / 1.171 Å, respectively. In general, these peaks were two to three orders of magnitude larger in XRD intensity than any other indexable Nb or Ti peaks. Precise lattice parameter measurements of these peaks yield lattice parameters of 3.311 Å for the pure Nb film and 3.001 Å for the a-axis of the Ti film, Table 2, which are equal to the bulk values within the estimated precision of the measurement (~0.2%). The c-axis measurement of 4.689 Å for the Ti film is about 1.7% larger than that expected for bulk

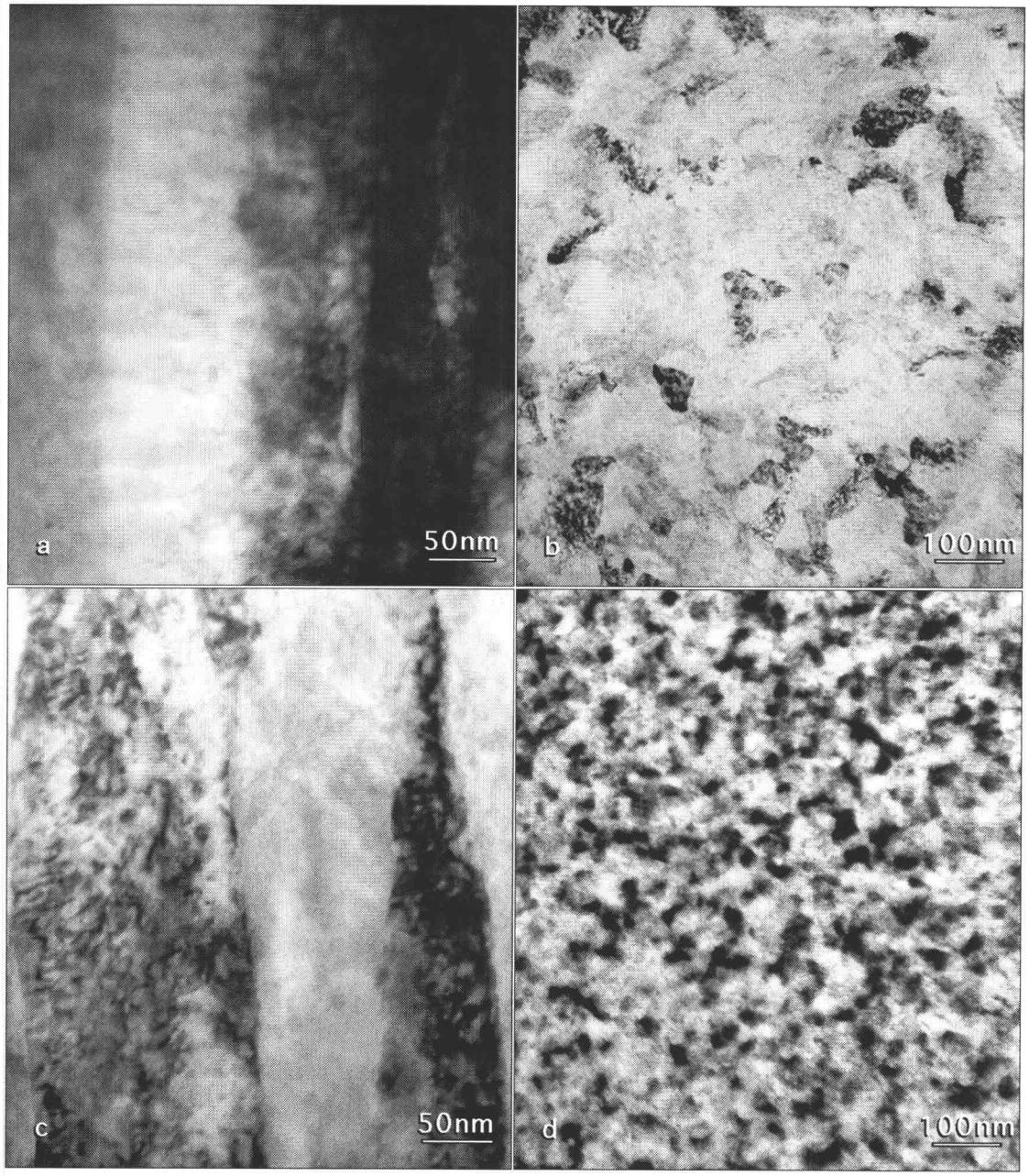

Figure 10. Bright field TEM images of the pure Nb and Ti films; a.) transverse view and b.) plan view of the pure Nb film, c.) transverse view and d.) plan view images of the pure Ti film, which correspond to the selected area diffraction images in Figure 11.

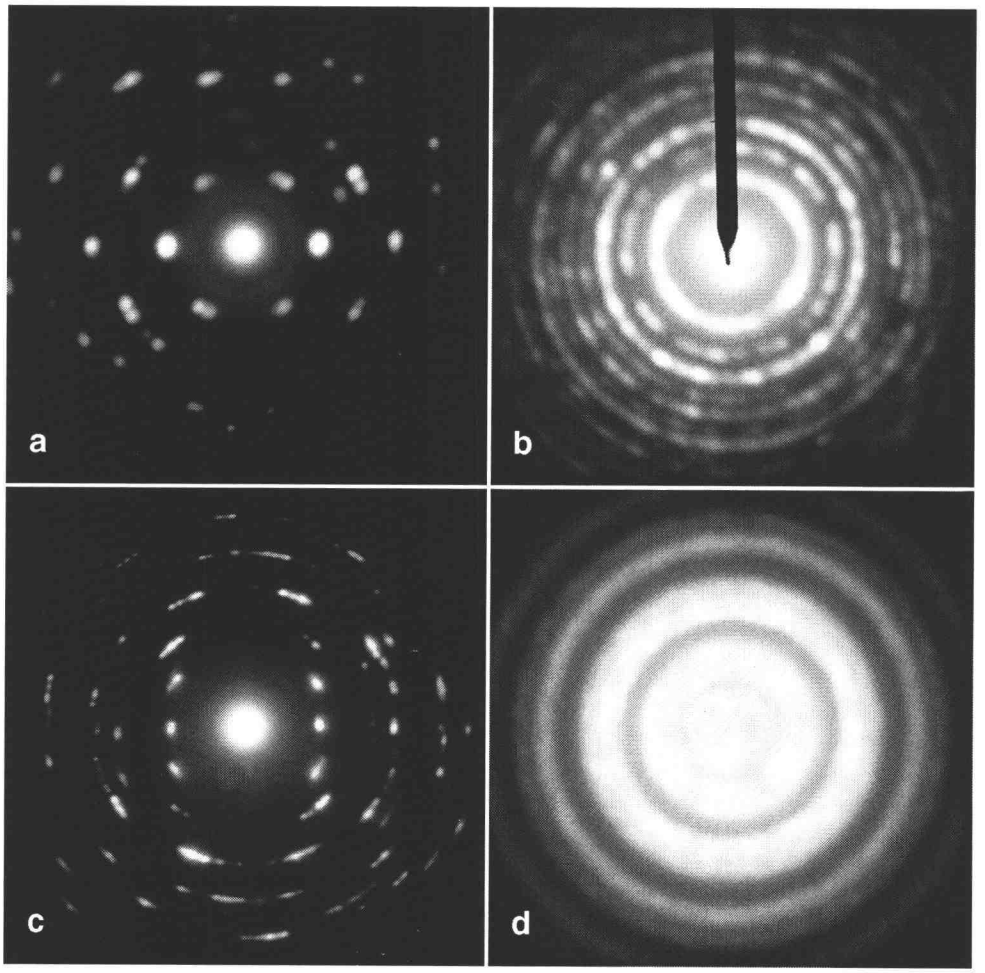

Figure 11. Transverse view, selected area diffraction images of the pure Nb and Ti films; a.) transverse view and b.) plan view of the pure Nb film, c.) transverse view and d.) plan view images of the pure Ti film, which correspond to the bright field images in Figure 10.

Ti. Finally, it should be noted that the pure Nb films deposited at the ambient temperature and at 200 °C had similar SAD patterns and identical (within 0.2%) measured lattice parameters.

Nb/Ti Multilayers

Transverse section TEM images of the Nb/Ti multilayers, with bilayer periods ranging over 5 orders of magnitude, are shown in Figures 12a-d. At the smallest bilayer period, ~1.7 nm, discrete, uniform Nb and Ti layers are found even when the designed Nb layer thickness (0.6 nm) is less than 3 atomic plane spacings (Figure 12a). The layers within a grain are parallel, but layers show misorientations up to 30° across adjacent columnar grains. The columnar grains appear to be crystallographically coherent over many bilayers. The Λ=17 nm Nb/Ti thin film is shown in Figure 12b. Again, the columnar grains show sharp, parallel, uniform layering with crystallographic coherence across many bilayers. Misorientations up to 20° are found between layers in adjacent grains. Figure 12c shows approximately one bilayer of the Λ=170 nm Nb/Ti thin film. Although the Nb/Ti interfaces are not as sharp as the Λ=1.7 nm and Λ=17 nm films, averaging the surface roughness across several grains results in highly parallel layers. The largest bilayer period Nb/Ti multilayer is a single bilayer approximately 15 μm in thickness. The Nb/Ti interface of the film is shown in Figure 12d. Columnar grains cross the Nb/Ti interface which is extremely rough relative to the smaller bilayer period Nb/Ti films.

Table 3 contains quantitative microstructural results of TEM layer thickness measurements and calculated film compositions along with quantitative EMPA measurements of the film composition. The measurements of bilayer period may be compared to bilayer periods calculated from low angle XRD peaks in Table 2. For the Λ=1.7 nm film the TEM and XRD measurements of 1.8 nm and 1.63 nm for the bilayer

Table 2. XRD and SAD crystallographic structure results

	XRD measurements				SAD patterns Transverse View	
Film Set	Λ [nm]	Nb a_o [Å]	Ti a [Å]	Ti c [Å]	Image Type	Structure
pure Ti	x	x	3.001	4.689	spot	HCP
pure Nb[a]	x	3.311	x	x	spot	BCC
Λ=1.7 nm	1.63	3.306	2.928	4.670	spotted-ring	BCC
Λ=17 nm	13.6	3.300	2.905	4.679	spotted-ring	BCC&HCP
Λ=170 nm	x[b]	3.300	2.927	4.663	spot	BCC&HCP
Λ=15,000 nm	x[b]	3.310	2.987	4.673	spot	BCC&HCP
(Nb/Ti)/Ti	x	3.296	2.916	4.776	spot	BCC&HCP
Λ=17 nm 1hr/300°C	13.4	3.304	x[c]	x[c]	spot	BCC&HCP
Λ=17 nm 10hr/450°C	14.4	3.315	x[c]	x[c]	spot	BCC&HCP
Λ=17 nm 1hr/600°C	x	3.348	x	x	ring	BCC

[a] This film was fabricated with a substrate temperature of 200 °C.
[b] The dimensions of these measurements are either too large or too small for the measurement technique.
[c] The presence of only two diffraction peaks {0002} and {0004} led to an incomplete solution to the HCP lattice parameters.

Table 3. TEM and EMPA layer thickness and bulk composition results

	TEM measurements					
Film Set	Grain Size [nm]	d_s [nm]	d_n [nm]	Λ [nm]	Bulk Composition [wt%Ti]	EMPA [wt%Ti]
pure Ti	17	x	x	x	100	
pure Nb[a]	33	x	x	x	0	
Λ=1.7 nm	17	0.6[c]	1.2[c]	1.8	x[b]	50
Λ=17 nm	17	3.7	10	13.7	59	63
Λ=170 nm	16	66.4	101.8	167.9	45	
Λ=15,000 nm	x	x[b]	x[b]	x[b]	x[b]	
(Nb/Ti)/Ti	11	18.4	36.2	54.9	70	75
Λ=17 nm 1hr/300°C	x	4.1	9.6	13.7	59	
Λ=17 nm 10hr/450°C	16	6.3	7.8	14.1	59	
Λ=17 nm 1hr/600°C	41	x	x	x	x	

[a] This film was fabricated with a substrate temperature of 200 °C.
[b] The dimensions of these measurements are either too large or too small for the measurement technique.
[c] These measurements based on EMPA composition measurements.

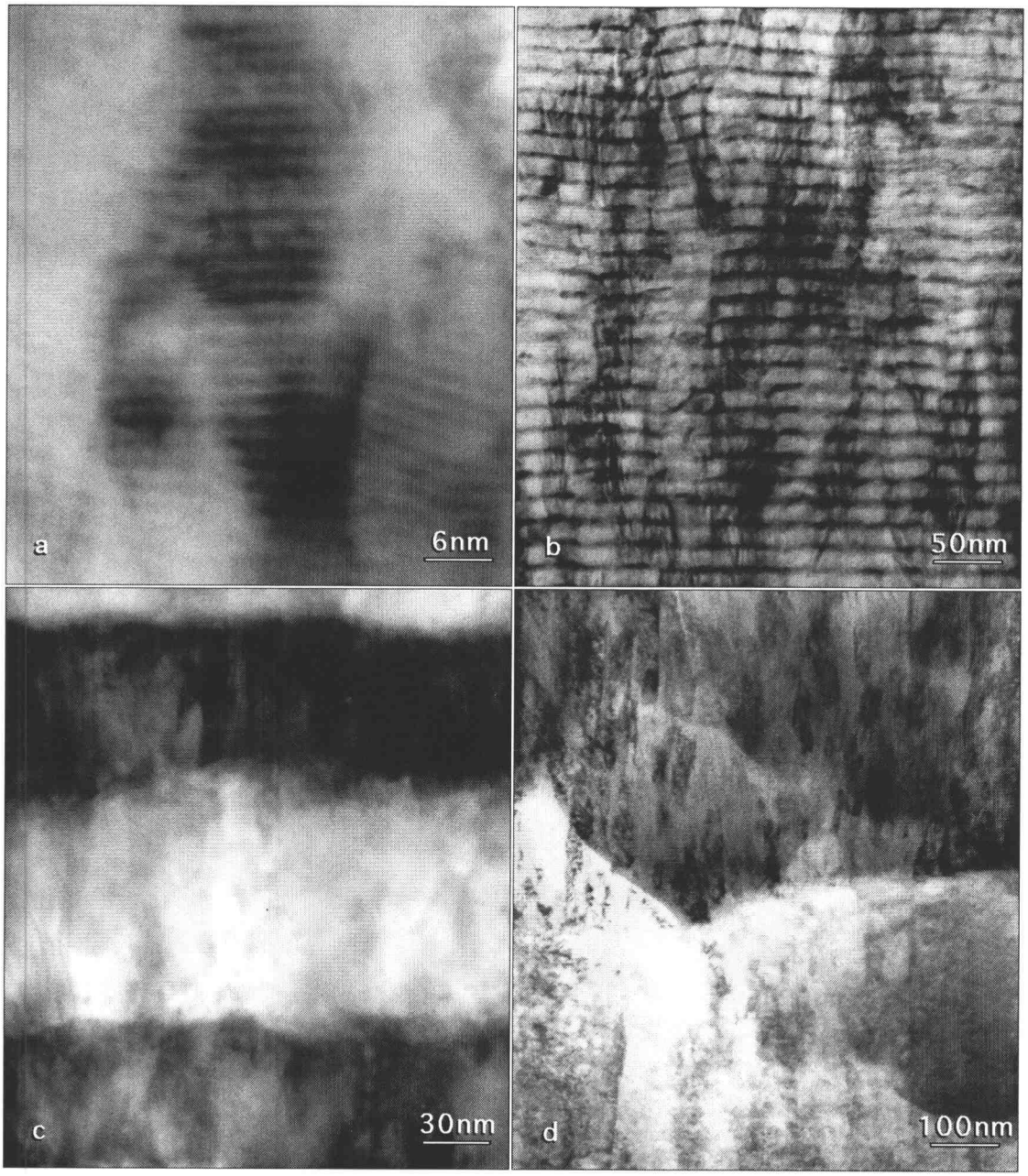

Figure 12. Transverse view, bright field TEM images of the Nb/Ti multilayered films; a.) Λ=1.7 nm, b.) Λ=17 nm, c.) Λ=170 nm and d.) Λ=15,000 nm. In the micrographs, the dark and light layers correspond to the Nb and Ti layers, respectively.

period, respectively, are within 10% of the designed bilayer period. Also, calculations of the Nb/Ti thickness ratio, based on the EMPA composition measurement of Nb50wt%Ti for the Λ=1.7 nm film are within 10% of the designed thickness ratio. The Λ=17 nm film shows good agreement between the TEM and XRD measurements of 13.7 nm and 13.6 nm for the bilayer period, respectively, although both of these measured values of the bilayer period were about 20% lower than the design value. TEM measurement of the individual layers shows that the Nb layer thickness is almost 40% less than the design value while the measured Ti layer thickness of 10 nm is close to the design value of 10.7 nm. The calculated bulk composition of Nb59wt%Ti is in good agreement with the EMPA measurement of Nb63wt%Ti, but about 20% higher than of the designed composition of Nb47wt%Ti. TEM measurements of the layer thicknesses, bilayer period and the resulting bulk composition for the Λ=170 nm film are all with 10% of the design values.

In all the Nb/Ti multilayered films dominant Nb-BCC{110} and/or Ti-HCP{0002} and Nb-BCC{220} and/or Ti-HCP{0004} XRD peaks are found, as seen in an example XRD plot of the Λ=17nm film in Figure 13. SAD images of the Nb/Ti films confirm that in all cases except for the Λ=1.7 nm film, the XRD peaks are indeed a combination of both the Nb-BCC and the Ti-HCP crystal structures. The measured lattice parameters for all of the Nb/Ti films are within 1.6% of expected bulk values.

(Nb/Ti)/Ti Multilayer

A transverse view image of the (Nb/Ti)/Ti multilayered film is shown in Figure 14. The periodicity in the β-layer sublattice is clearly visible with sharp interfaces between the Nb and Ti layers. Texturing is shown by the long columnar grains which are coherent over several α/β-superlattice periods. There is a slight misorientation, up to 10°,

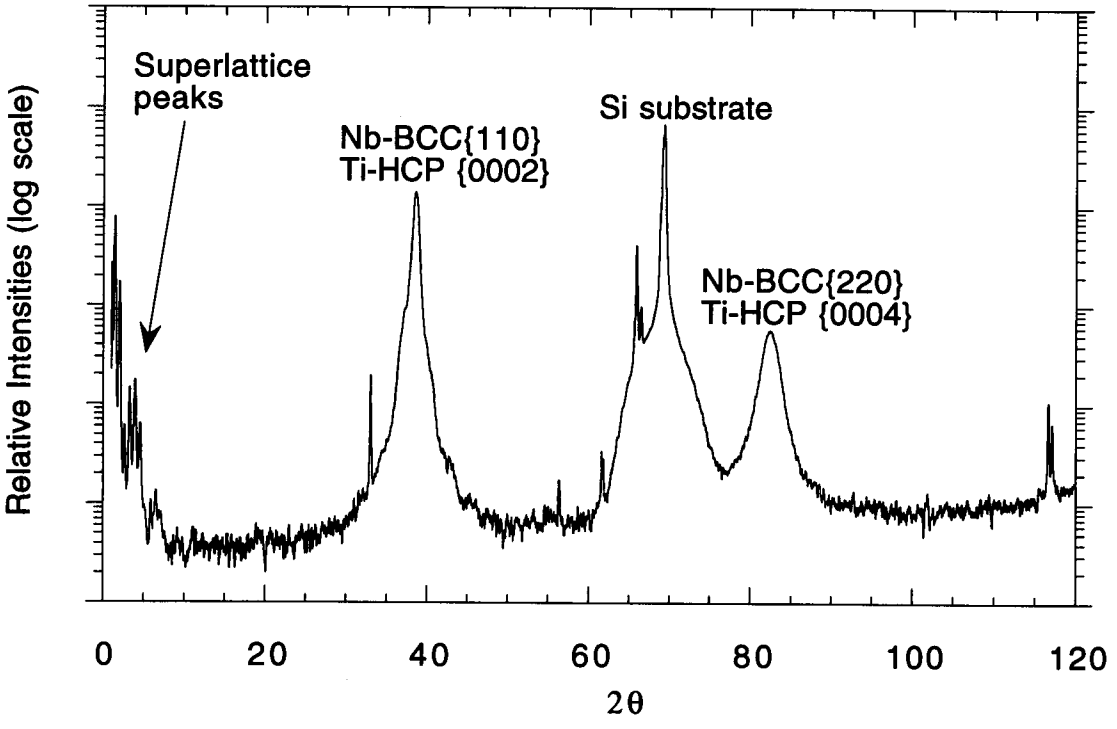

Figure 13. An XRD intensity profile of the Λ=17nm film.

between layers in adjacent columnar grains, but there is very little layer roughness inside individual grains. TEM measurements show the α-layer and β-layer thickness and the β-layer thickness ratio to be 18.4 nm, 36.2 nm and 1:1, respectively. The thickness ratio of Nb/Ti in the β-layer is off by almost a factor of three and thickness of both the α and β-layers are off about 25% from the design values which makes the composite well off the design composition of Nb47wt%Ti. The composition of the film based on TEM measurements is Nb70wt%Ti which is in good agreement with the composition of Nb75wt%Ti measured by EMPA. The SAD pattern in the inset of Figure 14 clearly shows a textured, two-phase BCC and HCP structure. This is again in agreement with the dominant peaks in the XRD traces which yield lattice parameters within 2% of bulk Nb and Ti values.

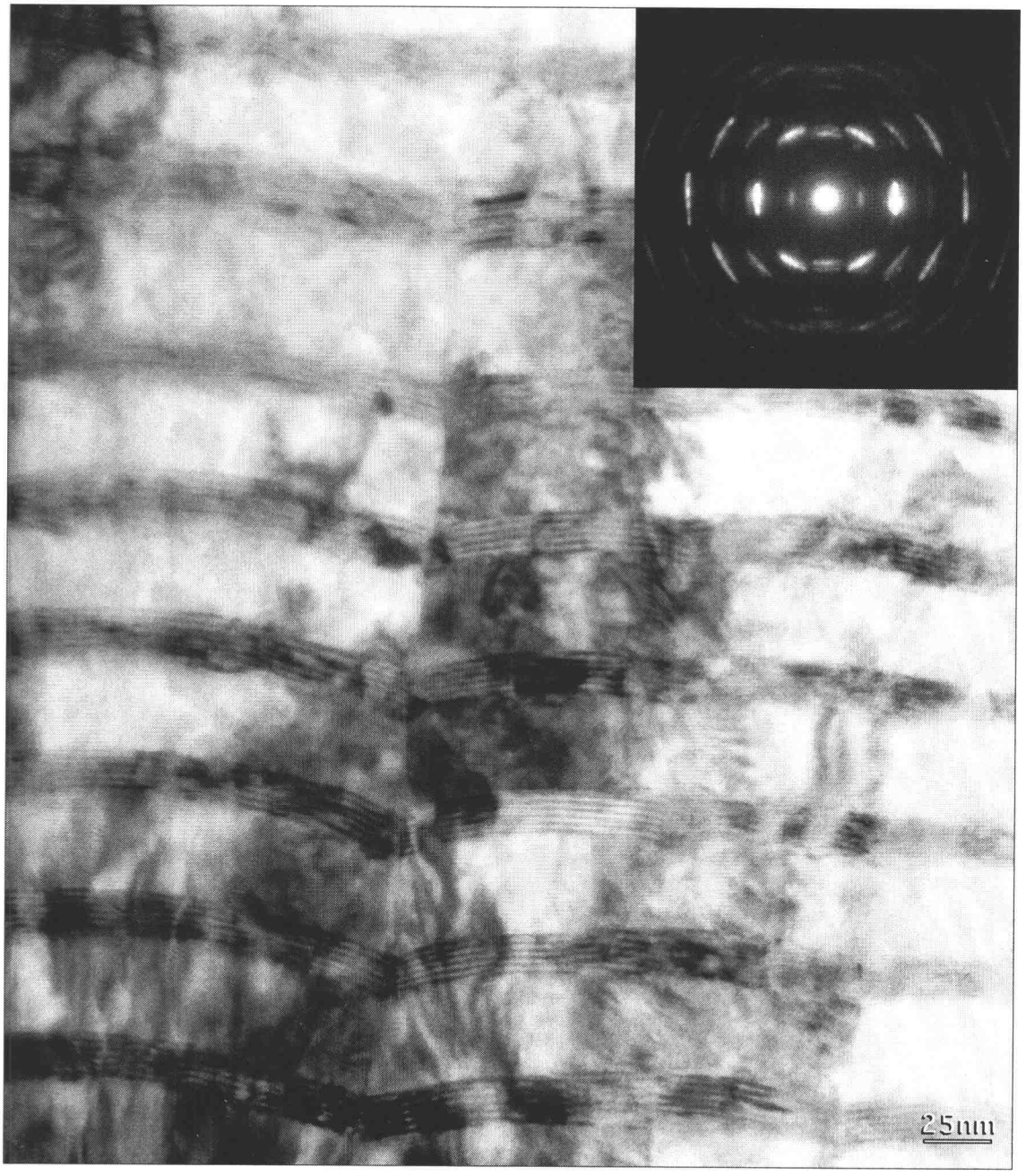

Figure 14. A transverse view, bright field and selected area diffraction (inset) images of the of the (Nb/Ti)/Ti film. In the micrograph, the dark and light layers correspond to the Nb and Ti layers, respectively.

Heat Treated Nb/Ti Multilayers

The heat treated, Λ=17 nm film, transverse BF and SAD images are shown in Figures 15 and 16, respectively. Although the BF images of the No Heat Treatment NHT and 1 hr/300 °C, Figures 15a and 15b respectively, show little difference in the appearance of the bilayered microstructure, the SAD patterns of the two samples are distinctly different. The NHT SAD pattern, Figure 16a, shows a diffuse ring pattern which indicates a lower crystal order and/or less texturing in the film relative to the discretely spotted SAD pattern of the 1 hr/300 °C specimen, Figure 16b. With increasing heat treatment time and temperature, a change in the appearance of the bilayer structure can be detected. At 10 hr/450 °C, Figure 15c, the bilayer period is more diffuse than the 1 hr/300 °C sample, yet still clearly evident. The SAD pattern of the 10 hr/450 °C sample, Figure 16c, has a more dominant BCC pattern relative to the 1 hr/300 °C sample which indicates a formation of an interdiffused BCC Nb-Ti forming at the expense of the pure Nb and Ti layers. At 1 hr/600 °C the bilayer period, as well as the texturing of the film, has been destroyed by interdiffusion. This can be seen in the equiaxed grains of the BF image, Figure 15d, as well as the SAD ring-pattern, Figure 16d, which represents a crystal lattice of randomly oriented BCC grains. An interdiffused Nb-Si layer was observed by TEM at the film/substrate interface in both the 1 hr/600 °C and 10 hr/450 °C films. In the 1 hr/600 °C film, the usual single XRD peak at BCC{110} and HCP{0001} planes was split into two peaks which is consistent with the formation of this Nb-Si interdiffusion layer [33].

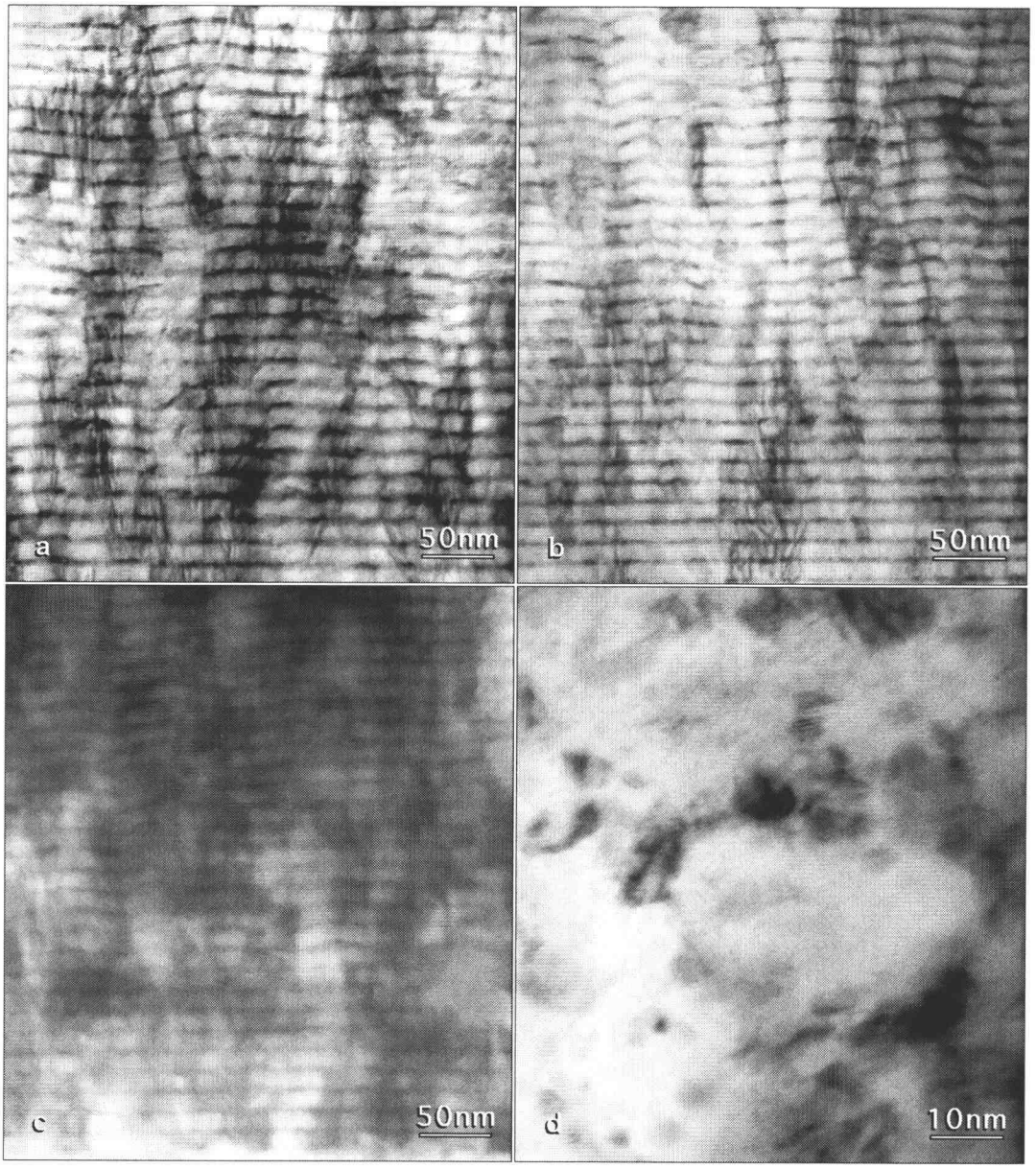

Figure 15. Transverse view, bright field TEM images of the heat treated, Λ=17 nm Nb/Ti multilayered films; a.) no heat treatment, b.) 1 hr/300 °C, c.) 10 hr/450 °C and d.) 1 hr/600 °C. In the micrographs, the dark and light layers correspond to the Nb and Ti layers, respectively.

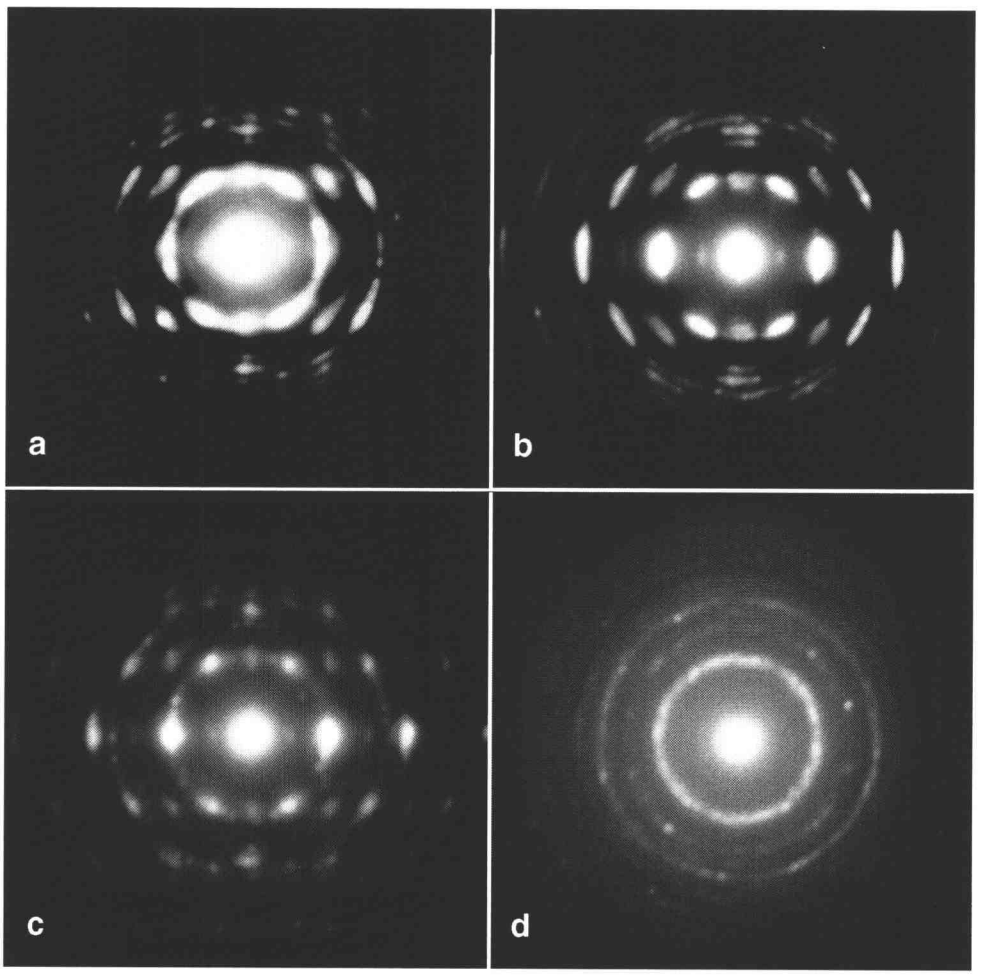

Figure 16. Transverse view, selected area diffraction images of the heat treated, Λ=17 nm Nb/Ti multilayered films; a.) no heat treatment, b.) 1 hr/300 $^{\circ}$C, c.) 10 hr/450 $^{\circ}$C and d.) 1 hr/600 $^{\circ}$C, which correspond to the bright field images in Figure 14.

Electromagnetic Characterization

Normal State Properties

The normal state resistivities at room temperature and 12 K are summarized graphically in Figures 17a and 17b, respectively. The plots show the resistivity of the films as a function of the Nb/Ti interface density (# Nb/Ti interfaces/nm) as well as values from the pure Nb and Ti films for comparison. The bilayer spacing controls the resistivity of the films. This can be seen in both the room temperature and 12 K plots, where there is an increase in the resistivity of the films with decreasing bilayer period (i.e. increasing Nb/Ti interface density). The plots also show that increasing the substrate deposition temperature reduces the resistivity of the films. At room temperature, the pure Nb and pure Ti films deposited at ambient substrate temperature have resistivities approximately twice as high as resistivities of bulk Nb and Ti [51]. In contrast, the pure Nb film deposited at 200 °C has a room temperature resistivity within 30% of bulk Nb. Furthermore, the Λ=17 nm sample is the only Nb/Ti multilayer film to be deposited at ambient substrate temperatures and is the only Nb/Ti multilayer film with a resistivity higher than the room temperature resistivity of cold-worked, bulk Nb47wt%Ti. Heat treatment of the Λ=17 nm films lowers its room temperature resistivity to the resistivity versus interface density curve of the Nb/Ti multilayers deposited at 200 °C.

Superconducting Properties

The superconducting properties of the films, as well as bulk Nb and Nb-Ti alloys, are summarized in H_{c2} versus T curves in Figures 18-20. The figures show the measured T_c and H_{c2}(4.2 K) points which serve as curve fit points to H_{c2}(T) curves, where

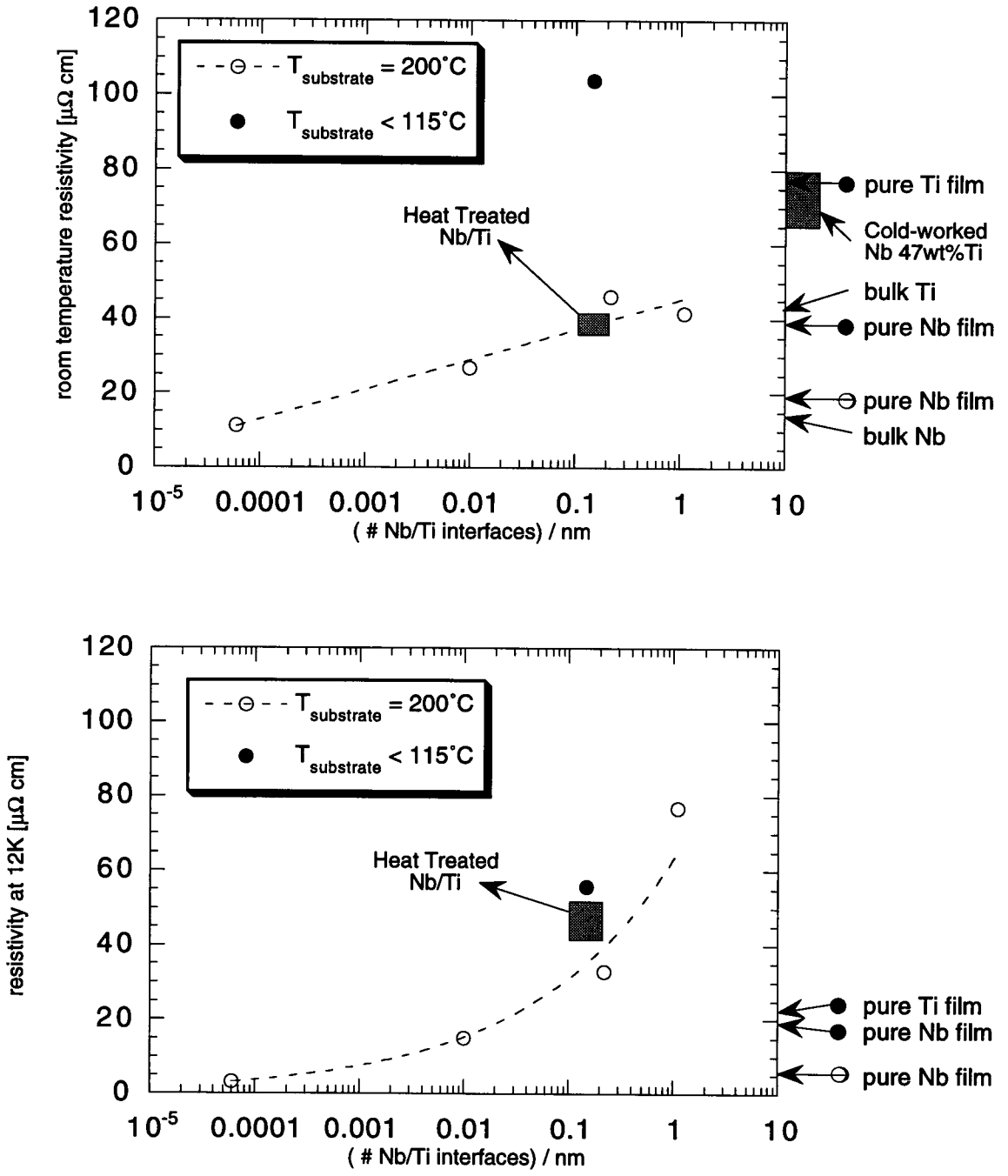

Figure 17. a.) Room temperature (upper graph) and b.) 12 K (lower graph) resistivity versus interface density (#Nb/Ti interfaces/nm) in the Nb/Ti films. Arrows connect the labels of the pure Nb and Ti films, along with bulk Nb, Ti and Nb47wt%Ti to their corresponding resistivity values. In the plots, hollow and filled circle data points represent film deposition temperatures of 200 °C and <115 °C, respectively.

$$H_{c2}(T) = H_o\left[1-\left(\frac{T}{T_c}\right)^2\right] \qquad \text{Equation 10}$$

and H_o is a fitting parameter which represents H_{c2} at absolute zero. The Λ=1.7 nm film had the highest J_c of ~2500 A/mm^2 at 3.5T, 4.2K (Figure 21). In all other cases, the J_c of the films (10-40 A/mm^2 at 5 T, 4.2 K) was approximately two orders of magnitude lower than critical current densities of conventional Nb-Ti superconducting wires (3000-4000 A/mm^2 at 5 T, 4.2 K).

The H_{c2} versus T curves of the two pure Nb films and bulk Nb are shown in Figure 18. The curves show a T_c of 9.0 K and 7.6 K for the Nb films deposited at 200 °C and ambient temperature, respectively. Thus the Nb film deposited at 200 °C has a T_c close (within 3%) to the observed T_c of bulk Nb (9.2 K), but the T_c of the Nb film deposited at ambient temperatures is about 17% lower than bulk Nb. The H_{c2} of both the pure Nb films fall in a range expected for heavily cold-worked, bulk Nb.

The superconducting properties of the Nb/Ti multilayered films are shown in Figure 19. At the smallest bilayer period, Λ=1.7 nm, the shape of the H_{c2} versus T curve qualitatively shows a similar behavior as the bulk Nb50wt%Ti curve [13], but both T_c and H_{c2}(4.2 K) of the film are depressed by almost a factor of two relative to the bulk alloy. The Λ=17 nm film was not superconducting above the lowest measured temperature of 4.2 K. At the larger bilayer periods, both the Λ=170 nm and Λ=15,000 nm films show H_{c2} versus T curves which closely match the curve of bulk Nb, not the curve of a bulk Nb-Ti alloy. The T_c (4.3 K) and H_{c2} (0.9T at 4.2 K) of the (Nb/Ti)/Ti film were 20% and 75% lower than a bulk material with the same overall composition. The H_{c2} versus T fitting curve of the (Nb/Ti)/Ti film was omitted because the T_c (4.3 K) was just above lowest measurable temperature of the system (4.2K), resulting in an unrealistic extrapolation.

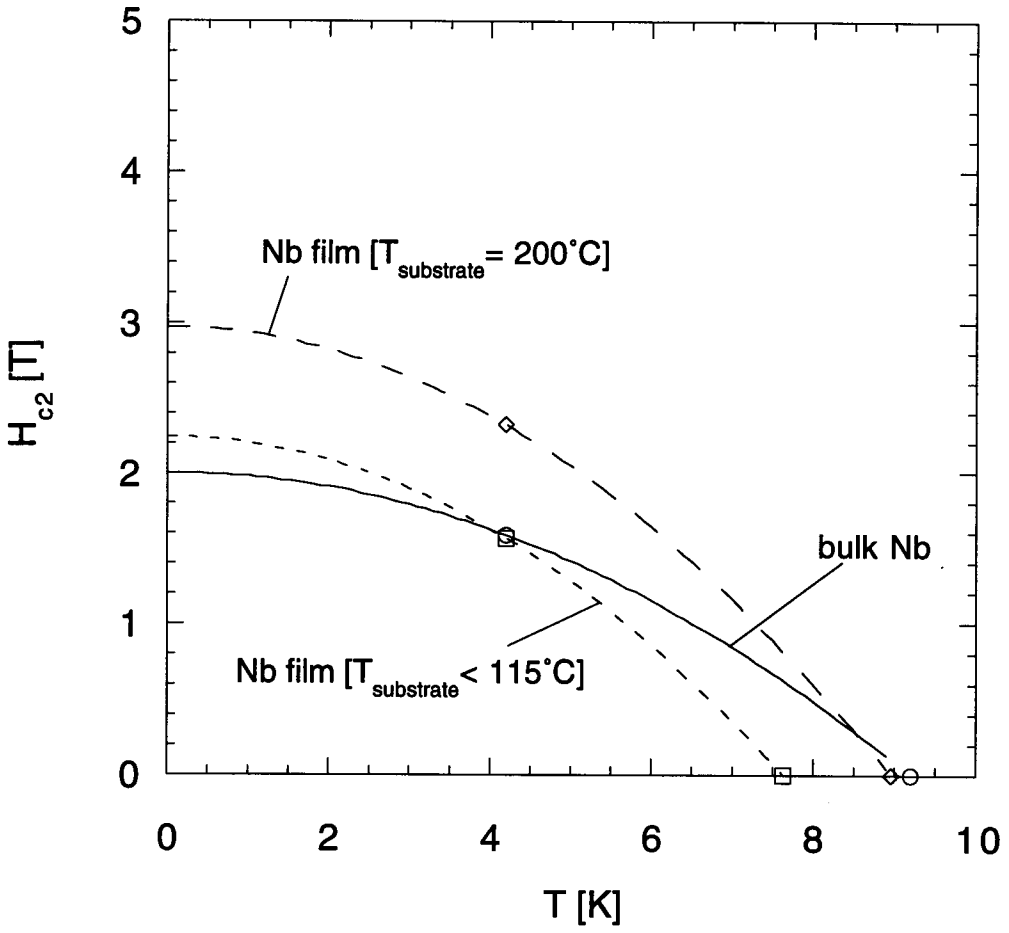

Figure 18. Measured and fit H_{c2} versus T curves of the pure Nb films.

The H_{c2} versus T curves of the heat treated multilayers thin film are shown in Figure 20. The 3 hr/400 °C curve represents the lowest heat treatment time and temperature at which the Λ=17 nm film is superconducting above 4.2 K. The 10 hr/450 °C film has a qualitatively similar H_{c2} versus T behavior to its equivalent composition (Nb63wt%Ti) bulk alloy, although the T_c and the H_{c2}(4.2 K) of the 10 hr/450 °C film are 8% and 29% lower, respectively, than the bulk alloy values. The 1 hr/600 °C film, which is the only film to have its bilayer periodicity destroyed by heat treatments, appears to have equal T_c and H_{c2} properties of bulk Nb63wt%Ti.

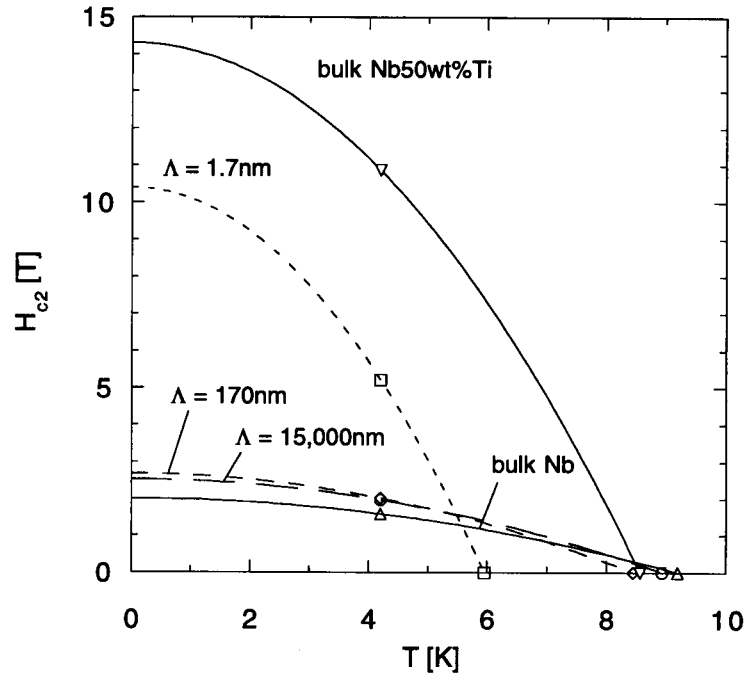

Figure 19. Measured and fit H_{c2} versus T curves of the Nb/Ti films.

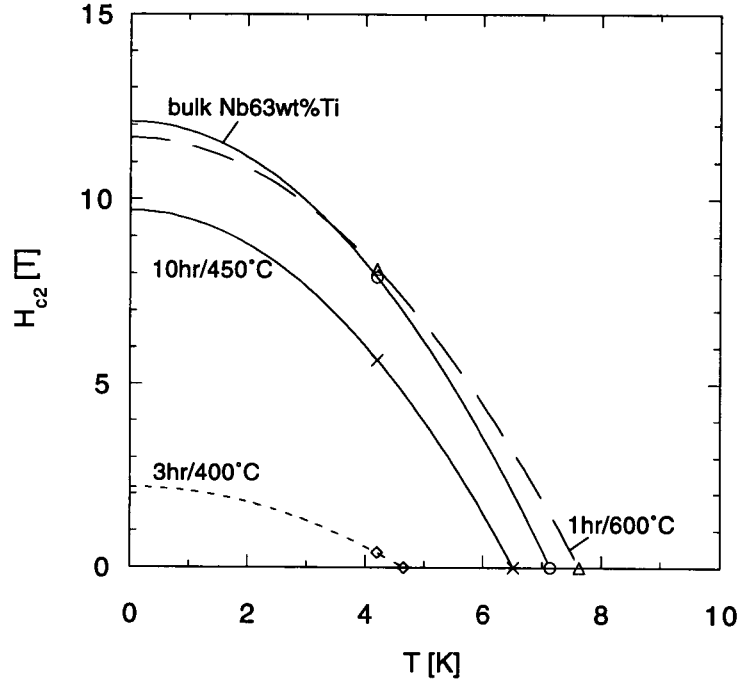

Figure 20. Measured and fit H_{c2} versus T curves of the heat treated Nb/Ti films.

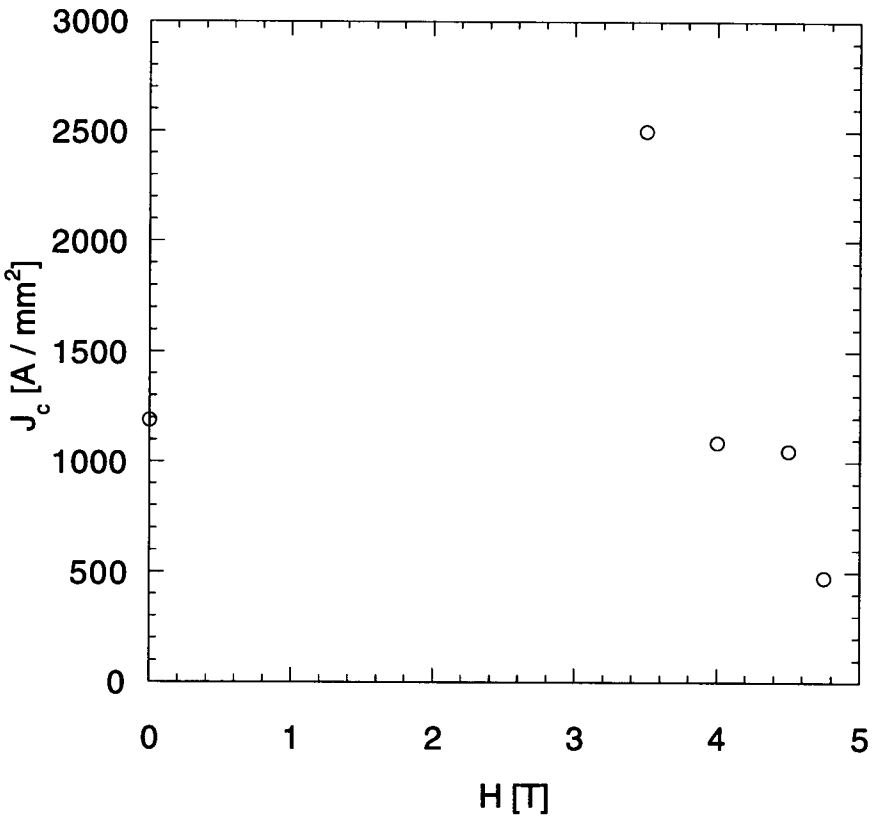

Figure 21. J_c versus H values for the Λ=1.7 nm film at 4.2K.

DISCUSSION

The motivation of this study was to design model microstructures which would lead to a better understanding of the interaction between the FLL and the microstructure of the superconductor. Furthermore, the information learned about the FLL/microstructure interactions could lead to the design of superconductors with higher J_c's. Unfortunately, depressed values of T_c and H_{c2} in the films, as well as measured critical current densities which were generally orders of magnitude less than conventionally fabricated Nb-Ti superconductors, changed the principal focus of this study. Thus, the focus of this study switched to understanding the effects of the microstructure and geometry of the film on T_c and H_{c2}.

Film Quality

Previous work on conventional and thin film Nb and Nb-Ti superconductors suggests two principal sources for the depressed superconducting properties of the films; film quality (disorder and contamination) and proximity effect coupling. The previous film quality and proximity effect coupling studies have focused principally on the relationship between the T_c and the microstructure or geometry of the film. In the film quality studies, contamination of pure Nb [52] and reduced crystal order [53-57], have been directly related to reductions in critical temperature. Proximity effect studies [28-29, 31, 45] have shown reductions in T_c and/or H_{c2} due to the sample geometry.

To assess the quality of our films, we compare the properties and the microstructures of the films to bulk superconductors of the same composition. For the purposes of this study, quality films are defined as films that achieve bulk properties. The two pure Nb films provide a good benchmark for both the microstructural and

electromagnetic quality of the films. Other than the texturing, the two pure Nb films are microstructurally equivalent to each other and to bulk Nb, in both crystal structure and lattice parameter. This suggests that the Nb films are microstructurally high-quality films. The room temperature resistivity of the Nb deposited at 200 °C is equivalent to bulk values. The resistivity of the Nb film deposited at ambient temperatures is nearly twice as high as bulk. Furthermore, the T_c of the Nb deposited at 200 °C is much closer to bulk values than the Nb film deposited at ambient temperatures. Therefore, we conclude the Nb film deposited at 200 °C is a higher quality film than the Nb film deposited at ambient temperature.

From this assessment of the quality of the Nb films, we can draw the following conclusions which we will use to evaluate the origin of the depressed properties in the Nb/Ti multilayer thin films. First, since the Nb films have no multilayer structure, proximity effect depression of T_c is ruled out as a source of T_c reduction. Next, the slight reduction in T_c (0.2 K) of the 200 °C Nb film may be due to approximately 1000 ppm of oxygen contamination [52] but this level is within the processing specifications of conventional Nb-Ti wire composites [9] and is considered negligible. This leaves the crystal order as the remaining factor controlling the properties in the Nb films.

Lattice strains can develop in the films due to a lattice mismatch between the substrate and the deposited film [57]. Also, it is well known that a higher substrate temperature provides more thermal/kinetic energy to the deposited atoms allowing the atoms to find an equilibrium position more easily relative to the lower substrate temperatures, thus producing a lower strain, higher quality film. T_c and resistivity results from the pure Nb films in this study achieve bulk properties, therefore high crystal order can be obtained in the Nb films with the use of a 200 °C substrate deposition temperature. We conclude that the electromagnetic characterization (T_c and resistivity) of the films provides a more sensitive measurement of the crystal order than XRD. This is a

reasonable assessment based on the fact that resistivity measurements are commonly more sensitive to the effects of cold-working of a bulk metal than XRD measurements.

Nb/Ti Films

To assess the quality of the Nb/Ti films, we revisit the same issues affecting the pure Nb films; contamination, crystal order and proximity effect. Based on the conclusions from the pure Nb films, contamination should have a negligible effect on the superconducting properties of the Nb/Ti films. This conclusion is supported by the fact that the H_{c2} versus T curve of the Λ=17 nm film heat treated for 1 hr/600 °C is equivalent to the bulk Nb-Ti alloy. This suggests that little or no contamination occurred during either the initial film deposition or subsequent heat treatment of the thin films.

Based on their low room temperature resistivities, we conclude that all the Nb/Ti films, except for the Λ=17 nm film, have a high-crystal order. This conclusion is supported by both SAD and XRD measurements which show the films to be essentially equivalent to bulk Nb-Ti. The Λ=17 nm film, however, has a high resistivity and the SAD pattern suggests a lower crystal order than the other Nb/Ti films. This was the only Nb/Ti film deposited at ambient substrate temperatures, which suggests that the low crystallographic order occurred during film deposition. The resistivity and SAD patterns of the heat treated Λ=17 nm films show that the disordering can be thermally recovered with heat treatments as low as 1 hr/300 °C.

With negligible degradation of superconducting properties due to contamination and low crystal order, proximity effect coupling is left as the principal factor controlling the superconducting behavior of the Nb/Ti films. Proximity effect calculations of T_c versus Λ using the Ledvij trilayer model [28] are shown in Figure 22 along with the corresponding measured values of the Nb/Ti films from this study (a detailed description of the calculations is included in the Appendix). The calculations, which are free of

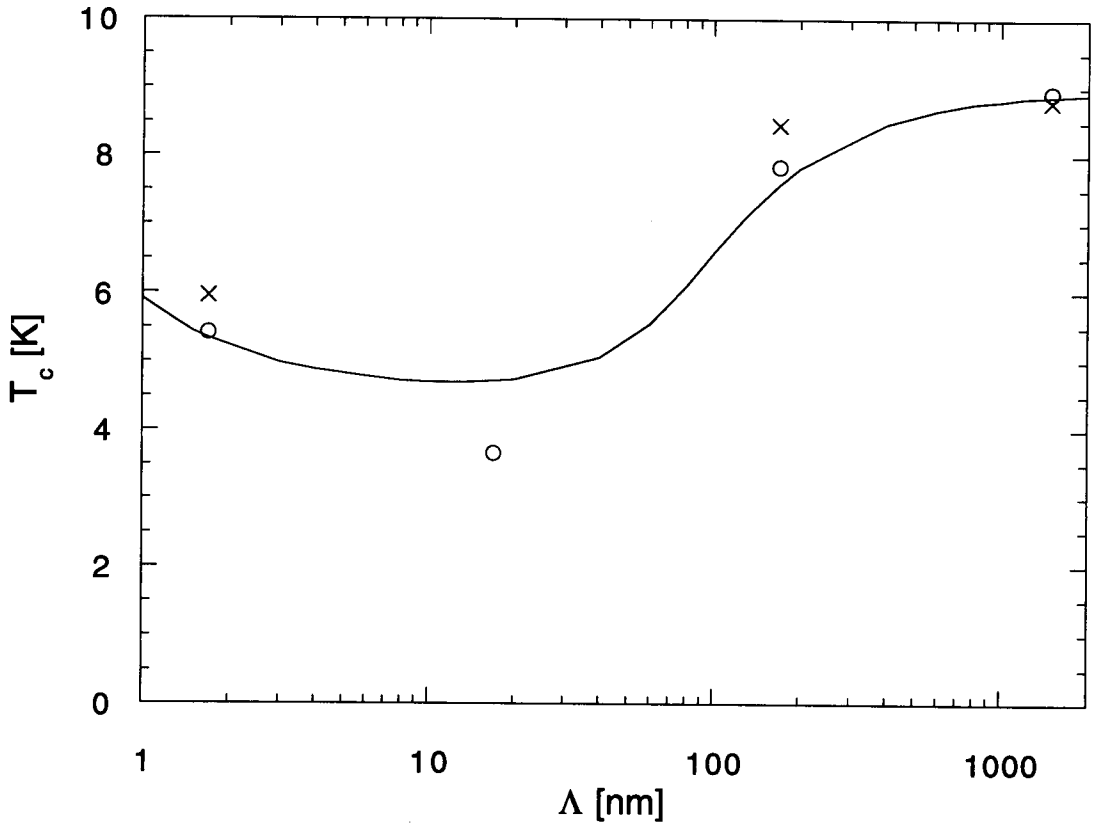

Figure 22. Calculated and experimental T_c versus Λ curves and data for the Nb/Ti series of multilayered films. The measured values of T_c are denoted with "X" and the calculated values, using TEM, XRD and EMPA data on layer geometries (see Appendix), are denoted with "O". The solid line corresponds to the calculated T_c of a series of Nb/Ti with a thickness ratio, d_s/d_n of 0.5.

fitting parameters, are in excellent quantitative agreement with the measured values of T_c versus bilayer period. For the Λ=1.7 nm film, the proximity effect calculations and the SAD patterns imply that a substantial amount of the bilayer period is an alloy phase BCC Nb-Ti. This is quite reasonable considering the size scale of this film. If each Nb/Ti interface in this film were a one atom-thick Nb50at%Ti alloy layer, the Nb-Ti alloy layer would account for approximately 25% of the total bilayer period.

The calculated T_c of 3.7 K for the Λ=17 nm film is in agreement with the fact that this film is not superconducting above 4.2 K. In the Λ=170 nm film, the model shows the onset of decoupling between the Nb/Ti layers, as the properties of the film approach

those of pure Nb. In the Λ=15,000 nm film, the calculations show the decoupling of the Nb and Ti layers is complete and the film acts as bulk Nb. These calculations are in excellent agreement with the measured properties of their corresponding films. Finally, the proximity effect model was also successful in qualitatively predicting the increasing T_c in the Λ=17 nm films with increasing heat treatment, assuming an increasing Nb-Ti interdiffusion layer with increasing heat treatments. Quantitative predictions of the heat treated films are hampered by unreliable measurements of the interdiffusion layer thickness and composition.

A second proximity effect model, by Takahashi and Tachiki [45], is used to help understand the H_{c2} behavior of the Nb/Ti films. Figure 23 shows the h_{c2} versus t behavior predicted by the Takahashi model for films with qualitatively comparable properties and geometries to the Nb/Ti films in this study. In the figure, h_{c2} is the reduced critical field of the film, where $h_{c2} = (H_{c2\text{-film}} / H_{c2\text{-bulk superconductor}})$ and t is the reduced temperature, where $t = (T / T_{c\text{-bulk superconductor}})$. The reduced critical temperature of the films, t_c, is defined as the intercept of the h_{c2} curve with the abscissa. At the largest bilayer period, d_s/ξ_{ns}=10, (the model assumes that d_s=d_n), the Takahashi model predicts only a slight reduction in T_c and H_{c2} of the film relative to the constituent bulk superconductor. The calculated h_{c2} versus t curve of the Takahashi model (solid line) closely follows the (dashed) curve

$$h_{c2} = t_c(1-(t/t_c)^2) \qquad \text{Equation 11}$$

which represents bulk H_{c2} versus T behavior scaled proportionately to the reduced critical temperature, t_c, of the film. Thus, if the critical temperature of the film were 95% of the T_c of the bulk superconductor, in the absence of a magnetic field, Equation 11 would calculate an H_{c2} for the film which was 95% of the H_{c2} of the bulk superconductor at absolute zero. Thus, according to Takahashi, reductions in the T_c of the film due to the proximity effect will be accompanied by proportional reductions in H_{c2} of the film. This

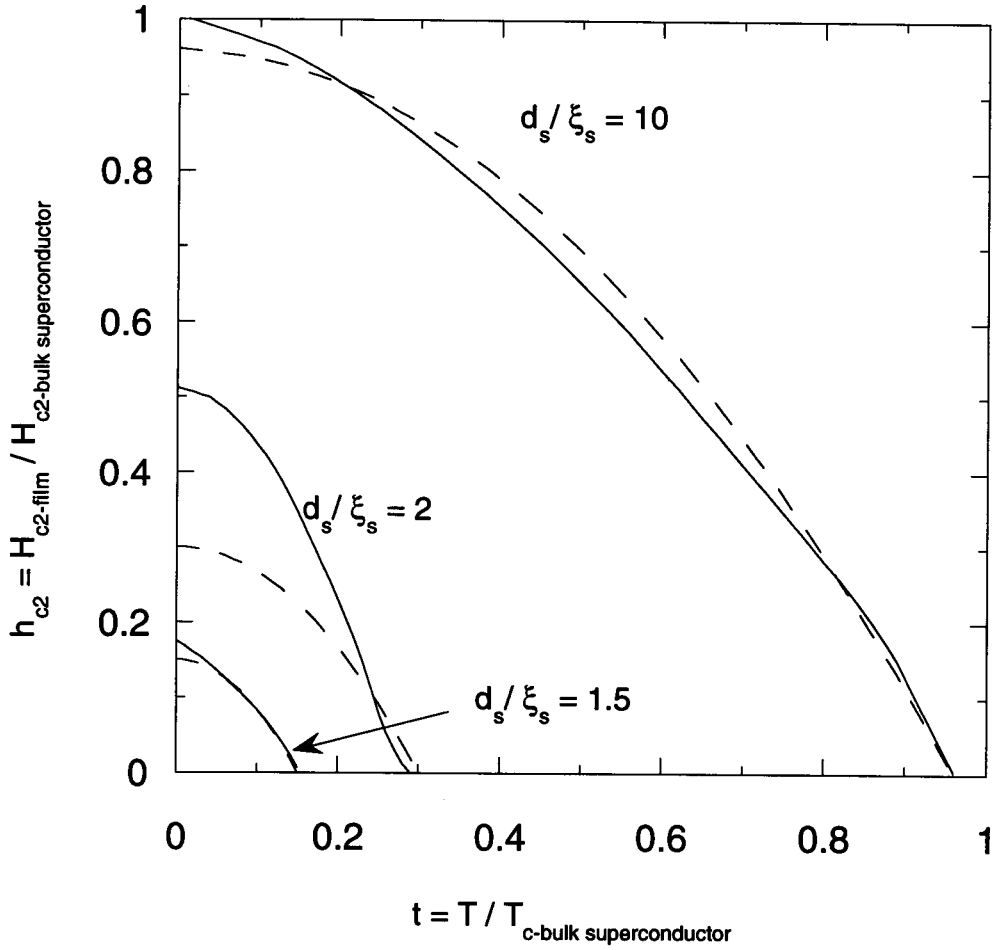

Figure 23. Reduced critical field, h_{c2}, versus reduced temperature, t, based on the Takahashi and Tachiki [45] proximity effect model (solid lines) and the equation; $h_{c2} = t_c (1 - (t / t_c)^2)$, (dashed lines) where t_c is the reduced critical temperature.

behavior is also seen at the smallest bilayer period, d_s/ξ_s=1.5, where 80% reductions in the T_c of the film are accompanied by similar reductions in the H_{c2} of the film. These large reductions at the smallest Λ are expected in the Takahashi theory because the theory uses a bilayer period model which does not account for properties of the film approaching bulk Nb-Ti alloy properties due to the presence of an interfacial Nb-Ti layer. At d_s/ξ_s=2, the predicted h_{c2} versus t curve diverges from the curve in Equation 11. Takahashi and Tachiki attribute this increase in H_{c2} to surface superconductivity in the thin superconducting layers which are decoupled from the normal layers. The increase in H_{c2}

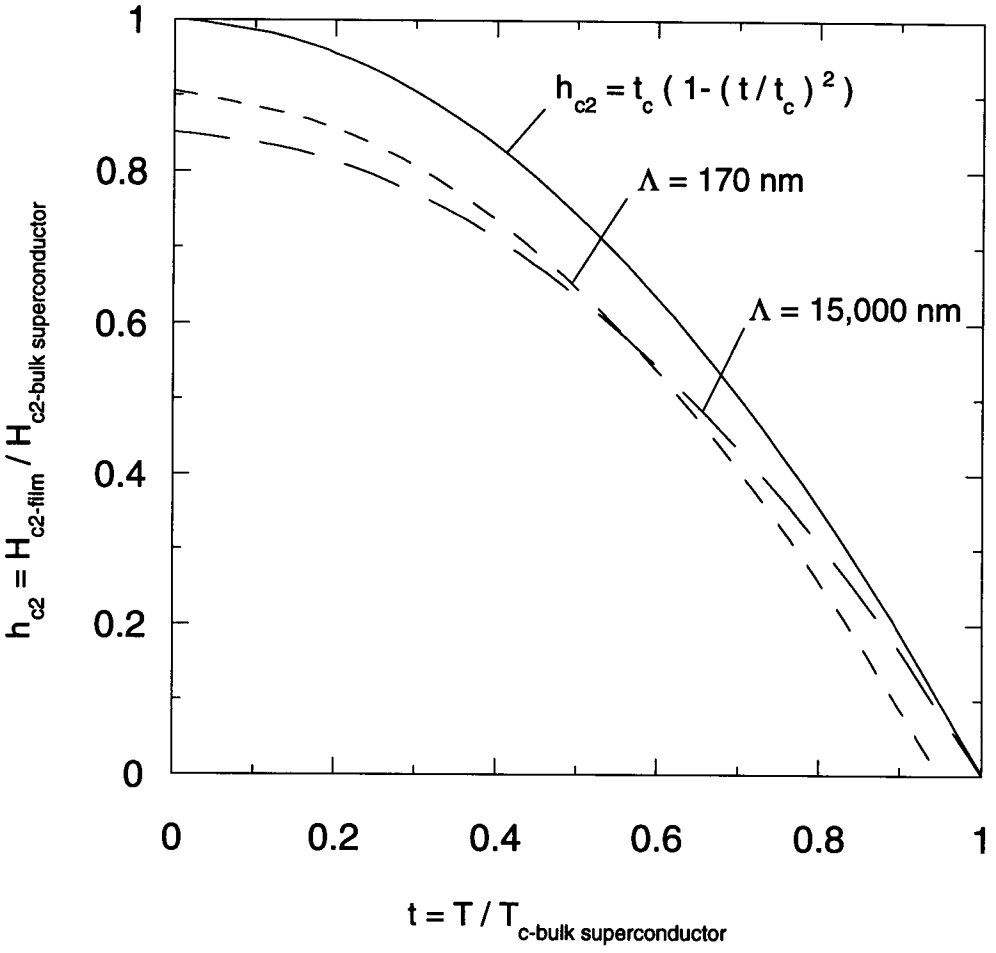

Figure 24. Reduced critical field, h_{c2}, versus reduced temperature, t, of the Nb/Ti films. The solid line represents the equation; $h_{c2} = t_c (1 - (t / t_c)^2)$ of the pure Nb film deposited at 200 °C. The properties of the Λ=170 nm and Λ=15,000 nm films have been scaled to the pure Nb film.

due to surface superconductivity is undesirable since it is accompanied by reductions in J_c of the system [5].

The reduced critical field versus reduced temperature behavior of the Nb/Ti films in this study is shown in Figure 24. The Λ=170 nm and 15,000 nm films have been scaled using the critical properties of the pure Nb film deposited at 200 °C. The h_{c2} versus t behavior of the Λ=170 nm and 15,000 nm films supports both the Takahashi and Ledvij proximity effect models which suggest, that with these film geometries, the Nb layers decouple from the Ti layers to produce a film which behaves like bulk Nb.

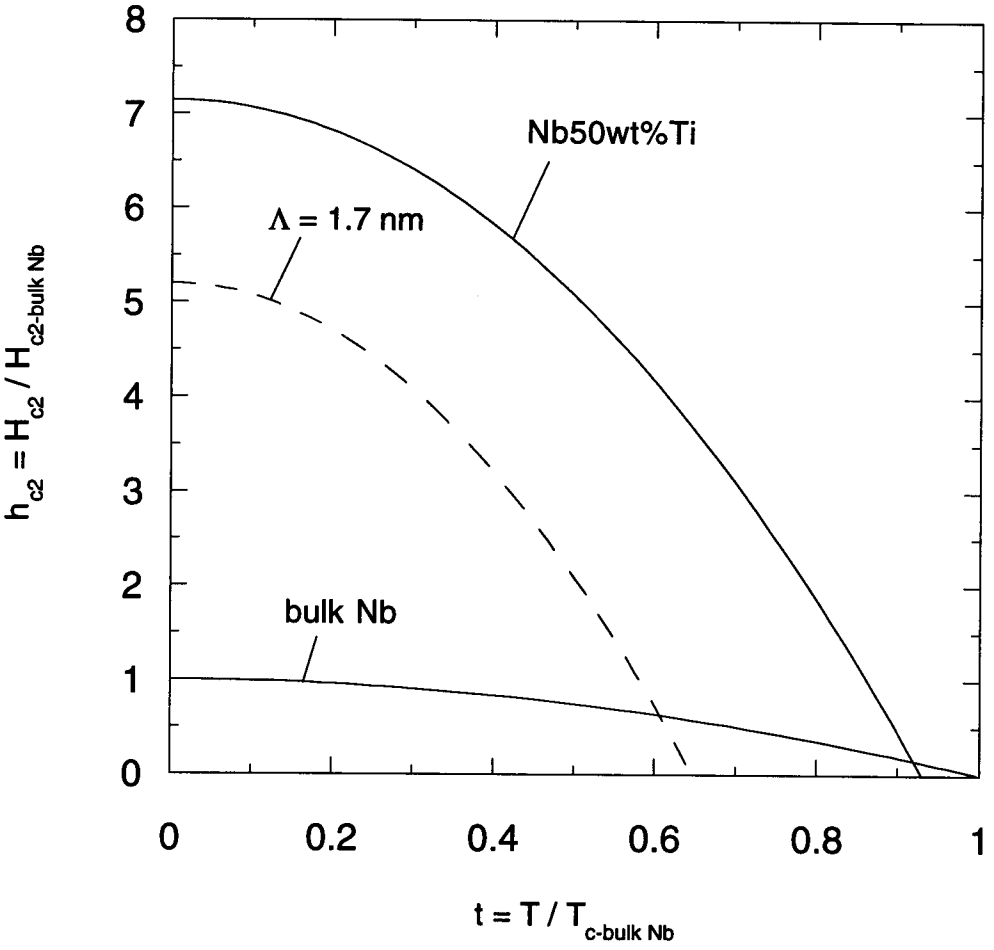

Figure 25. Reduced critical field, h_{c2}, versus reduced temperature, t, of the Λ=1.7 nm film. The solid lines represent the equation; $h_{c2} = t_c (1 - (t / t_c)^2)$ of pure Nb and Nb50wt%Ti, scaled to pure Nb properties.

The h_{c2} versus t behavior of the Λ=1.7 nm film is compared to bulk Nb and bulk Nb50wt%Ti in Figure 25. The figure illustrates that the h_{c2} versus t behavior of the film is qualitatively more similar to the alloy than the pure Nb. This is further evidence that the Nb-Ti interface is controlling the properties in this film. The reductions in H_{c2} and T_c of the film relative the bulk alloy due to the proximity effect are consistent with the layered geometry of the film.

Thus, the H_{c2} behavior of the Nb/Ti films is consistent with the Takahashi proximity effect model. The model shows that reductions in the T_c of the multilayered

films relative to the bulk properties of the superconducting layer will be accompanied by proportional reductions in H_{c2} of the film. With the complimentary Ledvij proximity effect model, quantitative modeling of the H_{c2} and T_c behavior of the Nb/Ti thin films can be achieved. A calculation of the T_c versus Λ behavior of the film using the Ledvij model, provides both the T_c of the film as well as the contribution of a interface alloy layer as a function of bilayer period as seen in Figure 6. At large bilayer periods ($\Lambda \geq \xi_s$), the H_{c2} of the film can be calculated using Equation 11, with the h_{c2} of multilayered thin film scaled to H_{c2} of the superconducting layer. At small bilayer periods ($\Lambda < \xi_s$), the H_{c2} of the film can be calculated using Equation 11, with the h_{c2} of multilayered thin film scaled to H_{c2} of the interface layer.

Conclusions

Based on the microstructural and electromagnetic properties of the films in this study, as well as calculations made from proximity effect models, we make the following conclusions;

1.) Deposition of the pure Nb and Nb/Ti multilayered films, at a substrate temperature of 200 °C, produces microstructurally high-quality films as determined by XRD, TEM BF and SAD images and resistivity measurements.

2.) The T_c and H_{c2} properties of the Nb/Ti films are all subject to proximity effect reductions in either T_c and/or H_{c2}. In the Λ=170 nm and Λ=15,000 nm films, the Nb layers decouple from the Ti layer, producing films which behave like bulk Nb. In the Λ=17 nm film, the proximity effect reduces T_c below our lowest measurable temperature of 4.2 K. In the smallest Λ film and the heat-treated films, a trilayer model as seen in Ledvij et al., is needed to properly describe the T_c and H_{c2} behavior. At Λ=1.7 nm, the properties of the film are qualitatively similar to bulk Nb-Ti due to a relatively large fraction of interface Nb-Ti in the bilayer period. Quantitatively

however, the film still has T_c and H_{c2} reductions due to the proximity effect. Similarly, the increasing thickness of the interface Nb-Ti with increasing heat treatment in the Λ=17 nm films, produces films with qualitatively correct H_{c2} versus T behavior. Unfortunately, the proximity effect depresses T_c and H_{c2} values relative to bulk Nb-Ti, until the bilayer period is eventually destroyed by interdiffusion.

3.) In all cases, the low J_c's of the films, relative to bulk alloys, were attributed to proximity effect reductions in T_c and/or H_{c2}.

Future Work

The initial goal of this study was to fabricate Nb/Ti multilayered films which modeled conventional Nb47wt%Ti wire composites. Plagued by the poor J_c performance in the films relative to the bulk alloys, the focus of the study turned to an understanding of the origins of the depressed properties. Using the results of this study, future work should return to the original goal of modeling the conventional Nb-Ti wire composites with Nb/Ti multilayered films which are not proximity effect limited and have interesting critical current densities.

Based on the results of this study and basic flux pinning theory, the approach in the design to model conventional Nb-Ti wire composites is to choose layer thicknesses that match the spacings between the fluxons in the FLL at a given field and then to use the proximity effect theories to choose layer compositions which are not subject to proximity effect reductions in T_c and H_{c2}. Basic core pinning models suggest that optimal flux pinning occurs when the pinning layer is approximately $2\xi_s$ and the superconducting layer is equal to the spacing between fluxons at a given field. Utilizing these design parameters while maintaining an optimal T_c and H_{c2} in the Nb-Ti system yields a 11 nm-Nb44wt%Ti/ 11 nm-Nb90wt%Ti and a 6 nm-Nb44wt%Ti/ 11 nm-Nb90wt%Ti multilayered film for 5 T and 8 T applied magnetic fields, respectively. Ledvij

calculations predict T_c's for both the films (see the Appendix) which are within 4% of the T_c of bulk Nb44wt%Ti.

Alternatively, surface pinning theory suggests that a maximum current density will result in a superconductor/normal layer geometry which maximizes the amount of superconducting material by spacing thin pinning layers ($d_n << \xi_s$) to match the FLL spacing at a given field. Again, maintaining optimal T_c and H_{c2} and designing for optimal flux pinning using a basic surface pinning model yields a 22 nm-Nb44wt%Ti/ 0.2 nm-Nb90wt%Ti and a 17 nm-Nb44wt%Ti/ 0.2 nm-Nb90wt%Ti Ti multilayered film for 5 T and 8 T applied magnetic fields, respectively. Neither of the surface pinning films, due primarily to the dominant superconducting layer thickness, should show proximity effect reductions in T_c or H_{c2}.

BIBLIOGRAPHY

1. J. Bardeen, L. N. Cooper, J. R. Schrieffer, *Phys. Rev.*, 108, 1175 (1957).

2. V. L. Ginzburg, L. D. Landau, *J.E.T.P.*, 20, 1064 (1950).

3. A. A. Abrikosov, *J. Chem. Phys. Solids*, 21, 199 (1957).

4. L. P. Gor'kov, *J.E.T.P.*, 7, 505 (1958).

5. A. C. Rose-Innes, E. H. Rhoderick, *Introduction to Superconductivity,* Permagon Press, pg 118, (1988).

6. A. M. Campbell, J. E. Evetts, *Adv. in Phys.*, 21, 199 (1972).

7. H. Ullmaier, *Irreversible Properties of Type II Superconductors*, Springer-Verlag, Berlin (1975).

8. A. D. McInturff, *The Metallurgy of Superconducting Materials*, Chapter 3, Plenum, New York, (1980).

9. D. C. Larbalestier, *Niobium-Titanium Superconducting Materials*, Plenum, New York, (1981).

10. A. W. West, D. C. Larbalestier, *Met. Trans. A*, 15, 843 (1984).

11. Li Chengren, D. C. Larbalestier, *Cryogenics*, 27, 171 (1987).

12. P. J. Lee, D. C. Larbalestier, *Acta. Met.*, 35, 2526 (1987).

13. C. Meingast, P. J. Lee, D. C. Larbalestier, *J. Appl. Phys.*, 66(12), 5962 and 5971 (1989).

14. P. J. Lee, J. C. McKinnell, D. C. Larbalestier, *Adv. Cryo. Engr.*, 36, 287 (1990).

15. R. M. Scanlan, D. R. Dietrerich, P. McManaman, W. Ghiorso, *IEEE Trans. Appl. Superconductivity*, 3(1), 1358 (1993).

16. K. Matsumoto, Y. Tanaka, K. Yamafuji, F. Funaki, M. Iwakuma, T. Matsushita, *IEEE Trans. Appl. Superconductivity*, 3(1), 1362 (1993).

17. L. R. Motowidlo, B. A. Zeitlin, M. S. Walker, P. Haldar, J. D. McCambridge, N. D. Rizzo, X. S. Ling, D. E. Prober, *IEEE Trans. Appl. Superconductivity*, 3(1), 1366 (1993).

18. I. Itoh, T. Sasaki, S. Minamino, T. Shimizu, *IEEE Trans. Appl. Superconductivity*, 3(1), 177 (1993).

19. G. L. Dorofejev, E. Y. Klimento, S. V. Frolov, E. V. Nikulenkov, E. I. Plashkin, N. I. Salunin, *Proc. Ninth Int'l. Conf. on Magnet Technology*, 564 (1985).

20. D. R. Dietderich, S. Eylon, R. M. Scanlan, *Adv. Cryo. Engr.*, 38(b), 685 (1992).

21. H. C. Kanithi, P. Valaris, L. R. Motowidlo, B. A. Zeitlin, R. M. Scanlan, *Adv. Cryo. Engr.*, 38(b), 675 (1992).

22. K. DeMoranville, D. Yu, J. Wong, *IEEE Trans. Appl. Superconductivity*, 3(1), 982 (1993).

23. R. Zhou, S. Hong, W. Marancik, B. Kear, *IEEE Trans. Appl. Superconductivity*, 3(1), 986 (1993).

24. J. L. Murray, *Phase Diagrams of Binary Titanium Alloys*, ASM International, pg 189 (1990).

25. L. N. Cooper, *Phys. Rev. Letters*, 6, 89 (1961).

26. N. R. Werthamer, *Phys. Rev.*, 132, 2440 (1963).

27. P. G. de Gennes, *Rev. Mod. Phys.*, 36, 225 (1964).

28. M. Ledvij, L. Dobrosavljevic-Grujic, J. R. Clem, *Phys. Rev. B*, 38(1), 129 (1988).

29. N. Sato, *J. Appl. Phys.*, 67(12), 7493 (1990).

30. Y. J. Qian, J. Q. Zheng, B. K. Sarma, H.Q. Yang, J. B. Ketterson, J. E. Hilliard, *J. Low Temp. Phys.*, 49(3), 279 (1982).

31. Y. Obi, M. Ikebe, Y. Muto, H. Fujimori, *Jap. J. Appl. Phys.*, 26(3), 1445 (1987).

32. J. D. McCambridge, N. D. Rizzo, X. S. Ling, J. Q. Wang, D. E. Prober, *IEEE Trans. on Appl. Superconductivity*, 5(2), 1697 (1995).

33. W. H. Warnes, K. J. Faase, J. A. Norris, to be published in *Adv. Cryo Engr.*, 42, (1996).

34. M. G. Karkut, V. Matijasevic, L. Antognazza, J. M. Triscone, N. Missert, M. R. Beasley, Ø. Fischer, *Phys. Rev. Letters*, 60(17), 1751 (1988).

35. J. A. Norris, M. S. Thesis, Oregon State University, Corvallis, OR, 97331 (1996).

36. J. Aarts, K. J. de Korver, P. H. Kes, *Europhys. Lett.*, 12(5), 447 (1990).

37. P. Koorevaar, W. Maj, P. H. Kes, J. Aarts, *Phys. Rev. B*, 47(2), 934 (1993).

38. Y. Kuwasawa, U. Hayano, T. Tosaka, S. Nakano, S. Matuda, *Physica C*, 165, 173 (1990).

39. W. P. Lowe, T. H. Geballe, *Phys. Rev. B*, 29(9), 4961 (1984).

40. P. R. Broussard, D. Mael, *Phys. Rev. B*, 40(4), 2321 (1989).

41. P. R. Broussard, *Phys. Rev. B*, 43(4), 2783 (1991).

42. P. R. Broussard, T. H. Geballe, *Phys. Rev. B*, 35(4), 1664 (1987).

43. P. R. Broussard, T. H. Geballe, *Phys. Rev. B*, 37(1), 60 and 68 (1988).

44. D. Kumar, M. G. Blamire, R. Doyle, A. M. Campbell, J. E. Evetts, *J. Appl. Phys.*, 76(4), 2361 (1994).

45. M. Takahashi, S. Tachiki, *Phys. Rev. B*, 33, 4620 (1986).

46. M. Takahashi, S. Tachiki, *Physica B*, 169, 121 (1991).

47. P. Hirsch, A. Howie, R. Nicholson, D. W. Pashley, M. J. Whelan, *Eletron Mircoscopy of Thin Crystals*, Robert E. Krieger Pub., Malabar, (1977).

48. M. A. Wall, *Microscopy Research and Technique*, 27, 262 (1994).

49. R. Alani, J. Jones, P. Swann, *Mat. Res. Soc. Symp. Proc.*, 199, 85 (1990).

50. B. D. Cullity, *Elements of X-ray Diffraction*, Addision-Wesley, Reading, (1978).

51. C. Kittel, *Introduction to Solid State Physics*, John-Wiley and Sons, New York, (1986).

52. C. C. Koch, *Phys. Rev. B.*, 9(3), 888 (1974).

53. L. R. Testardi, J. M. Poate, H. J. Levinstein, *Phys. Rev. B.*, 15(5), 2570 (1976).

54. J. C. Villigier, J. C. Veler, *IEEE Trans. Mag.*, 19(3), 946 (1983).

55. D. W. Face, S. T. Ruggiero, D. E. Prober, *J. Vac. Sci. Technol.*, A1(2), 326 (1983).

56. S. T. Ruggiero, D. W. Face, D. E. Prober, *IEEE Trans. Mag.*, 19(3), 960 (1983).

57 G. Oya, M. Koishi, Y. Sawada, *J. Appl. Phys.*, 60(4), 1440 (1986).

58. M. Tinkham, *Introduction to Superconductivity*, Robert E. Krieger Pub., Malabar, (1985).

59. R. C. Weast, *Handbook of Chemistry and Physics,* CRC press, Boca Raton, (1990).

APPENDIX

LEDVIJ PROXIMITY EFFECT MODEL

This appendix contains the numerical analysis code and the input parameters used to calculate the T_c's of the films in this study, based on the theoretical model of Ledvij et al. [28]. The program was written in the LabVIEW 3.0 programming environment using the G-programming language.

In their proximity effect model, Ledvij et al. use an expansion of the Gor'kov equations of superconductivity in the dirty limit

$$\frac{-D}{2}\Pi \bullet (G\Pi F - F\Pi G) = \frac{\Delta}{2\pi h}G - F \qquad \text{Equation A1}$$

and

$$G^2 + |F|^2 = 1 \qquad \text{Equation A2}$$

where G and F are the Gor'kov Green's functions of the average, integrated Fermi energy, D is the diffusion coefficient, Δ is the order parameter, and $\Pi = \nabla - (2\pi i / \phi_o)A$, where A is the vector potential. The film geometries conform to the trilayer period Λ of

$$\Lambda = d_s + d_n + 2d_i \qquad \text{Equation A3}$$

where s, n and i correspond to the superconducting, normal and interface layer thicknesses. The reduced critical temperature of each layer j (j = s, n, or i) is $t_j = T/T_{cj}$, where T_{cj} is the critical temperature of each layer. Ledvij et al. develop a self-consistency relation (Ledvij Equation 4)

$$\ln(t_j) = \Psi(1/2) - \Psi\left(\frac{1}{2} + \frac{\rho}{t_j}\right), \qquad \text{Equation A4}$$

which defines the function $\rho=\rho(t_j)$. This expression relates the order parameter $\Delta(r)$ to the integrated Green's function of the Fermi energy F(r) as a function of position r, where

$$F(r) \propto \frac{\Delta(r)}{T_{cj}\rho(t_j)}. \qquad \text{Equation A5}$$

According to Ledvij et al., each layer of the trilayer period must conform to the equation

$$\Pi^2 F = -k^2 F \qquad \text{Equation A6}$$

where $\Pi = (\delta/\delta r)$. By separation of variables, F(r) = f(x,y)g(z) where x is normal to the plane of the films, the eigenvalues of Equation A6 become (Ledvij Equations 8a and 8b)

$$k_{s,i}^2 = \frac{2\rho(t_{s,i})}{\xi_{s,i}^2} \qquad \text{Equation A7a}$$

and

$$k_n^2 = \frac{-2\rho(t_n)}{\xi_n^2}. \qquad \text{Equation A7b}$$

Ledvij et al. define the boundary conditions as

$$f_s = f_i, \quad \frac{d}{dz}\ln g_s = \eta_s \frac{d}{dz}\ln g_i \qquad \text{Equation A8}$$

at the s/i interface and

$$f_n = f_i, \quad \frac{d}{dz}\ln g_n = \eta_n \frac{d}{dz}\ln g_i \qquad \text{Equation A9}$$

at the n/i interface, where $\eta_{s,n}$ is the resistivity of layer s,n divided by the resistivity of layer i. This leads to the condition (Ledvij Equation 12)

$$\begin{aligned}
1 = {} & \cos(k_s d_s)\cosh(k_n d_n)\cos(2k_i d_i) \\
& + \left(\frac{1}{2}\right)\left(\frac{k_i^2}{k_s k_n}\eta_s\eta_n - \frac{1}{\eta_s\eta_n}\frac{k_s k_n}{k_i^2}\right)\sin(k_s d_s)\sinh(k_n d_n)\sin^2(k_i d_i) \\
& + \left(\frac{1}{2}\right)\left(\frac{k_n}{\eta_n k_i} - \frac{k_i}{k_n}\eta_n\right)\cos(k_s d_s)\sinh(k_n d_n)\sin(2k_i d_i) \\
& + \left(\frac{1}{2}\right)\left(\frac{\eta_s k_n}{\eta_n k_s} - \frac{\eta_n k_s}{\eta_s k_n}\right)\sin(k_s d_s)\sinh(k_n d_n)\cos^2(k_i d_i) \\
& - \left(\frac{1}{2}\right)\left(\frac{k_s}{\eta_s k_i} + \frac{k_i}{k_s}\eta_s\right)\sin(k_s d_s)\cosh(k_n d_n)\sin(2k_i d_i)
\end{aligned} \qquad \text{Equation A10}$$

which has a non-trivial solution at the critical temperature of the system when combined with Ledvij Equations 4 and 8.

The calculating engine of the numerical fit concentrates on Ledvij Equations 4, 8, and 12, which corresponds to appendix Equations A4, A7 and A10, respectively. The engine starts a calculation loop (Figure A1) by taking a user-input "temperature of the system", T, and the parameters in Table A1. Based on these values, the value of ρ is calculated for each of the layers using the numerical approximation in "Eqn4approx.vi", (Figure A2) where the reduced temperature, t, is T_c of the layer over T, according to

Ledvij Equation 4 (Equation A4). The algorithm (Figure A3) then calculates the values, k in the sub-routine "KvalueEqn8.vi", for each layer from Ledvij Equation 8 (Equation A7). Next the program calculates a value for the right-hand-side (RHS) of Ledvij Equation 12 (Equation A10) in the sub-routine "Eqn12.vi" (Figure A4). If the calculated value "Eqn12.vi" equals the value of the left-hand-side (LHS) of Ledvij Equation 12, the T_c of the film is taken as T. Otherwise T is decreased by a user-input temperature step and the calculation loop is repeated until the LHS of Ledvij Equation 12 equals the RHS of Ledvij Equation 12, or until T equals a user-input end-temperature, as seen in Figure A1.

The principal parameters for the calculations are listed in Table A1. The values of T_c and H_{c2} (extrapolated to 0 K) of the superconducting and interface layers are the measured values of the pure Nb film (deposited at 200 °C) and the Λ=17 nm film heat-treated for 1 hr/600 °C, respectively. The T_c of Ti is taken from Rose-Innes [5] and the H_{c2} of Ti is calculated from the expression $H_{c2}=0.59*H_{c3}$, [58] where the H_{c3} of Ti is 0.27T [59]. The coherence length of each layer is calculated from the critical fields as

$$\xi_s = (\phi_o / 2\pi H_{c2})^{1/2} \qquad \text{Equation A11}$$

where ϕ_o is 2.067×10^{-15} Tm^2.

For the Λ=1.7 nm and Λ=17 nm films, the bilayer period measured by XRD, and the thickness ratio, d_s/d_n, based on EMPA compositional measurements are used to calculate the values of d_s and d_n. For the superconducting and normal layer thicknesses in the Λ=170 nm and Λ=15,000 nm films, the measured TEM and design values from Table 3 and Table 1, respectively, are used. In all the films, the interface layer, d_i, is chosen to be one monolayer of Nb-Ti alloy. The scattering factors, $\eta_{s,n}$ are taken as the ratio of the resistivity of the superconducting and normal layers to the resistivity of the interface

Table A1. Measured parameters used in the T_c versus Λ curve in Figure 22.

Layer	T_c [K]	H_{c2} [T]	ξ [Å]	d [Å]	η
superconducting	8.96	2.95	106		0.12
interface	7.63	11.65	53	2.3	
normal	0.4	0.16	454		0.43

layer, respectively. We use the measured 12 K resistivities of the pure Nb film (deposited at 200 °C), the Λ=17 nm film heat-treated for 1 hr/600 °C and the pure Ti film for the resistivities of the superconducting, interface and normal layers, respectively.

Critical temperature calculations of the films for the future flux pinning experiments are based on numerical fits of T_c, H_{c2} [13] and resistivity [51] data as a function of wt%Ti. The numeric approximation of the T_c versus wt%Ti curve is

$$T_c = 9.399 + 5.776x - 14.859x^2 \text{ [K]} \qquad \text{Equation A12}$$

where x is the wt%Ti and numeric approximation of the H_{c2} versus wt%Ti curve is

$$H_{c2} = 0.384 + 30.67x + 61.8x^2 - 231.76x^3 + 138.68x^4 \text{ [T] at 4.2 K} \qquad \text{Equation A13}$$

where x is the wt%Ti. The resistivity as a function of wt%Ti is based on a linear interpolation between the resistivity of pure Nb and pure Ti as

$$\text{resistivity} = 14 + 27x \text{ [} \mu\Omega\text{-cm]} \qquad \text{Equation A13}$$

where x is the wt%Ti. These numeric approximations yield the T_c, H_{c2} and resistivity values seen in Table A2, which were used in the Ledvij model to calculate the T_c of the future flux pinning film set.

Table A2. Parameters used in calculated T_c's of the future flux pinning films.

Layer	wt%Ti	T_c [K]	H_{c2} [T]	ξ [Å]	d [Å]	resistivity [μΩ-cm]	η
superconducting	44	9.06	14.4	48		26	0.82
interface	67	6.60	11.62	53	2.3	32	
normal	90	2.56	0.16*	454		38	1.18

* Due to the uncertainty of the H_{c2} in Ti rich alloys, the H_{c2} of the normal layer was chosen as the same value from Table A1 for pure Ti.

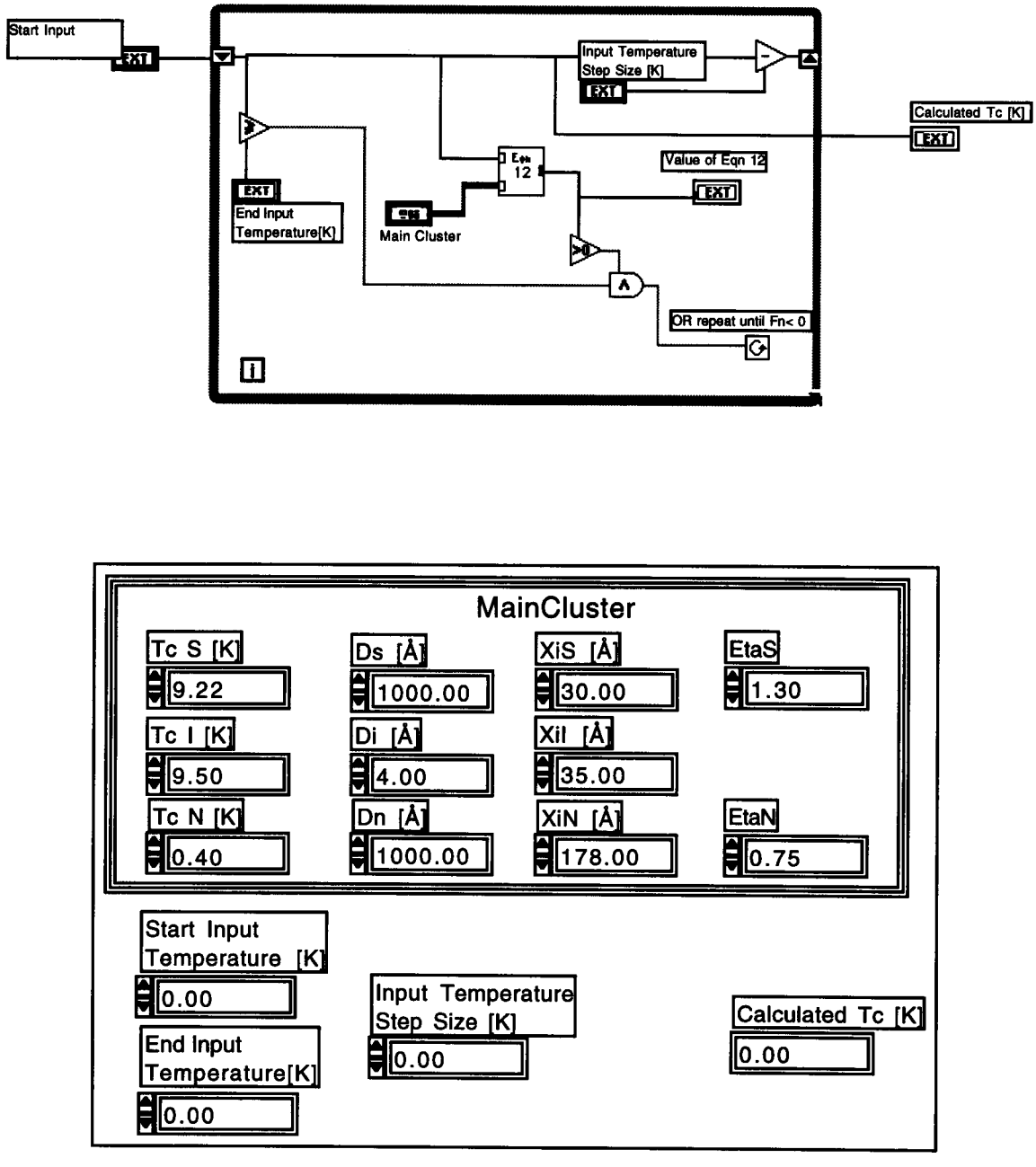

Figure A1. "The Ledvij 3.0.vi" a.) diagram and b.) front panel. The "Main Cluster" in the front panel corresponds to the "Main Cluster" icons of the "Ledvij 3.0.vi" and "Eqn12.vi" diagrams.

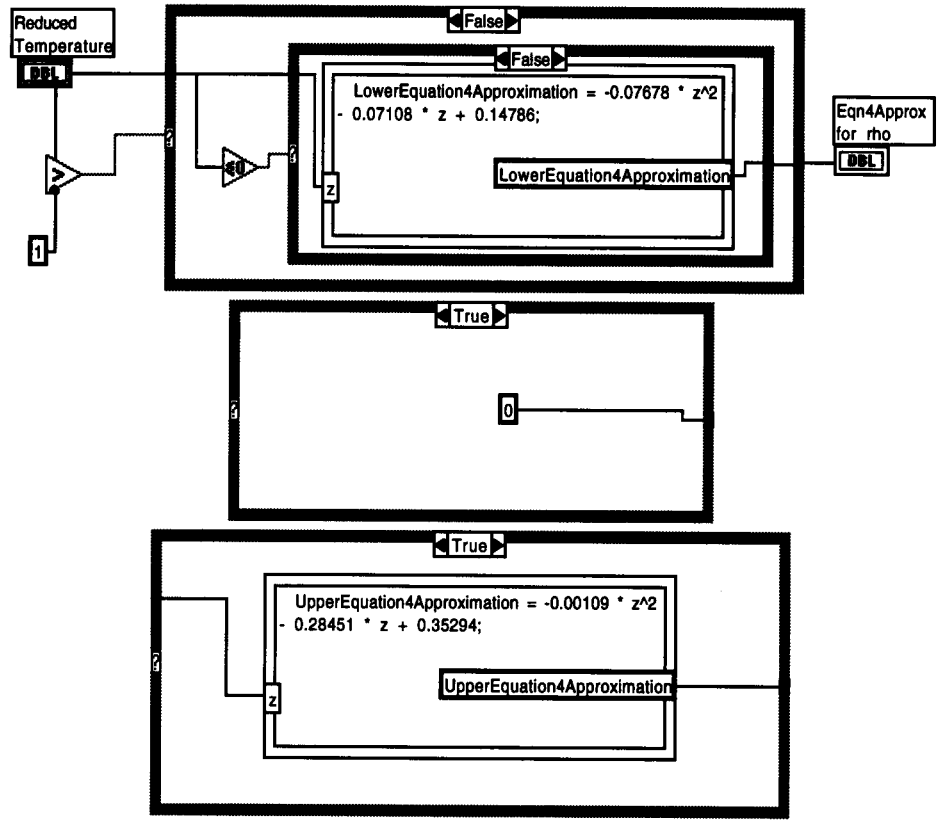

Figure A2. The "Eqn4Approx.vi" diagram.

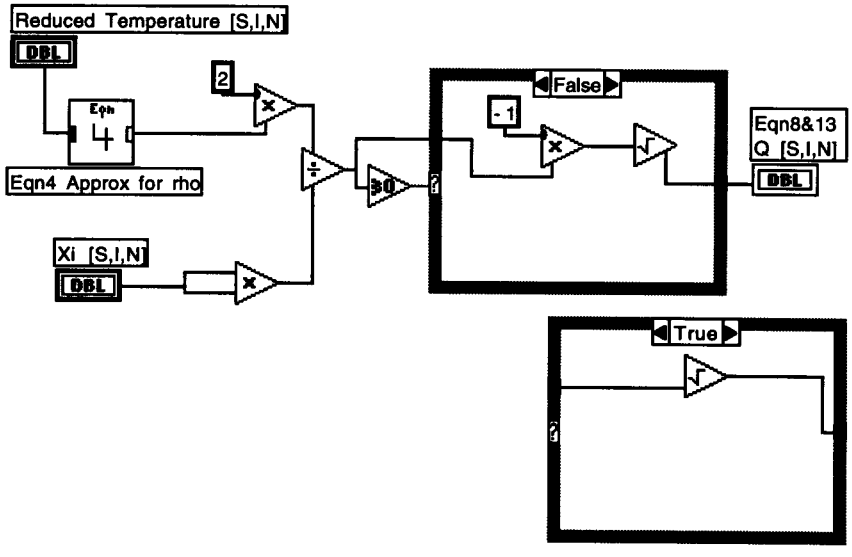

Figure A3. The "Eqn8.vi" diagram

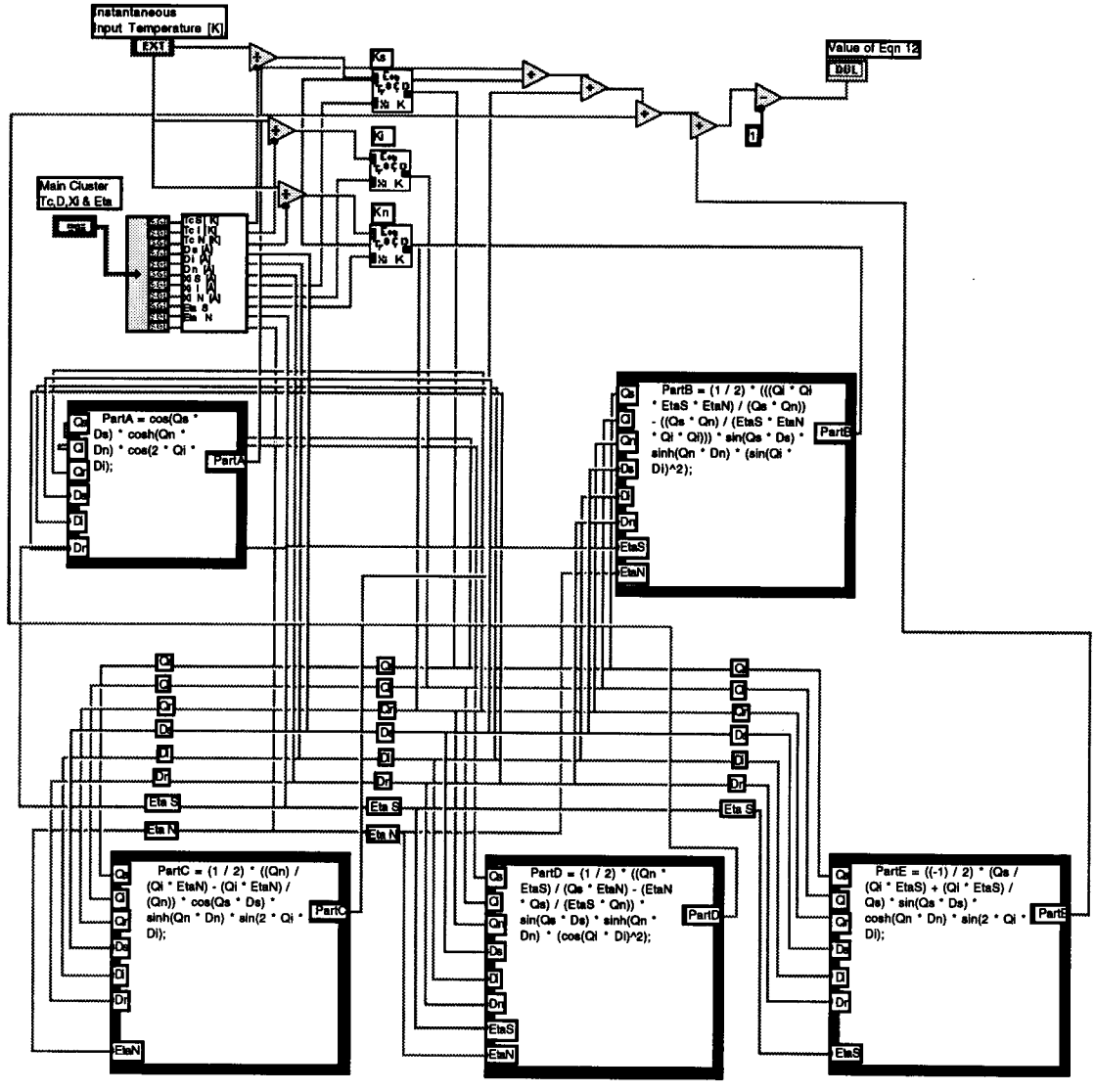

Figure A4. The "Eqn 12.vi" diagram.